

Rossby Wave Dynamics over South America Explored with Automatic Tropical–Extratropical Cloud Band Identification Framework

MARCIA T. ZILLI^a AND NEIL C. G. HART^a

^a *School of Geography and the Environment, University of Oxford, Oxford, United Kingdom*

(Manuscript received 12 January 2021, in final form 29 May 2021)

ABSTRACT: During austral summer, persistent tropical–extratropical cloud bands, such as the South Atlantic convergence zone (SACZ) over South America (SAm), link the tropical humid areas to the subtropics. In this study, we utilize an automatic object-based methodology to identify synoptic cloud band events occurring over SAm that are responsible for almost 60% of the precipitation during the rainy season (November–March). In addition to identifying SACZ events as cloud bands persisting 4 or more days, the framework also highlights the relevance of transient events (i.e., events persisting for 3 days or less) to the climatology. The location and persistence of the cloud band events are modulated by the propagation of synoptic-scale extratropical disturbances interacting with intraseasonal variability in the basic-state upper-level zonal wind. During persistent events (i.e., lasting 4 or more days), upper-level westerly anomalies over the subtropics favor the propagation extratropical disturbances deeper into the tropics. Conversely, transient events occur when the Bolivian high is displaced/expanded southeastward, bringing upper-level easterly winds into subtropical latitudes and blocking the propagation of Rossby waves into lower latitudes. Subsequent anomalous subtropical convection from the cloud bands result in sources of Rossby waves that interact with the basic flow, resulting in downwind enhancement or damping of the extratropical disturbances. The adopted methodology proved to be a powerful framework in demonstrating this interaction between scales, with the basic state influencing and being modified by the synoptic disturbances.

SIGNIFICANCE STATEMENT: Most of the summer precipitation in the dry subtropics of South America is sourced from tropical regions, such as the Amazon, and is transported poleward through continental-scale cloud bands. Here, we identify these cloud bands as well as the flow that supports the atmospheric waves responsible for their formation. This provides valuable information to understand the mechanisms associated with the location and persistence of these rainfall systems. We show that once these cloud bands form, they modify the atmospheric flow necessary for the traveling waves that created them in the first place. These insights are useful for evaluating the effects of climate change on this important dynamical source of rain, particularly in understanding the change predicted by climate models.

KEYWORDS: Atmosphere; South America; South Atlantic convergence zone; Rossby waves; Synoptic climatology

1. Introduction

Global satellite imagery during austral summer (December–February) indicates the presence of persistent cloud bands linking tropical humid areas to the midlatitudes through subtropical regions, which are generally under Hadley circulation subsidence. The convective activity from these tropical–extratropical cloud bands results in precipitation occurring in otherwise dry subtropical zones (Kodama 1992). Southern Hemisphere cloud bands occur over the South Pacific (Kiladis et al. 1989; Vincent 1994; van der Wiel et al. 2015), the South Atlantic (Nogués-Paegle and Mo 1997; Carvalho et al. 2011), and southern Africa (Harrison 1984; Washington and Todd 1999), with studies suggesting that their activity could be interconnected through the generation and propagation of Rossby waves (Grimm and Silva Dias 1995; Hart et al. 2010; Grimm and Reason 2015; Rodrigues and Woollings 2017).

Over South America (SAm), these cloud bands originate over the Amazon and extend southeastward toward subtropical South Atlantic (SATl) and are classified as South Atlantic convergence zone events when persisting for at least 4 days (SACZ; Nogués-Paegle and Mo 1997; Liebmann et al. 1999;

Carvalho et al. 2004, 2011; Gonzalez and Vera 2014; Zanin and Satyamurty 2020). In its active phase, the SACZ is associated with intense precipitation and the occurrence of natural disasters throughout its extension (Liebmann et al. 1999; Carvalho et al. 2004; Cavalcanti 2012; Zilli et al. 2017). In contrast, the absence of organized convection and SACZ events (sometimes referred to as the SACZ inactive phase) during the rainy season can lead to severe droughts, as observed in 2013–15 (Coelho et al. 2016a,b; Rodrigues and Woollings 2017; Rodrigues et al. 2019). During the inactive phase of the SACZ, precipitation is enhanced over southeastern SAm (SESA), favored by the transport of moisture from the Amazon to the region by the low-level jets (LLJs; Nogués-Paegle and Mo 1997; Gonzalez and Vera 2014; Mattingly and Mote 2017).

Most studies have identified the SACZ activity through statistical analysis isolating its principal modes of oscillation [usually through empirical orthogonal function (EOF) analysis] either on synoptic scales (Todd et al. 2003; van der Wiel et al. 2015) or, more frequently, on intraseasonal or longer time scales (Nogués-Paegle and Mo 1997; Robertson and Mechoso 2000; Carvalho et al. 2004, 2011; Cunningham and Cavalcanti 2006; Grimm and Zilli 2009; Gonzalez and Vera 2014; Grimm and Saboia 2015; Vera et al. 2018; Grimm 2019). Despite isolating statistically dominant characteristics, EOF analyses are limited to the first couple of modes, which usually explains less

Corresponding author: Marcia T. Zilli, marcia.zilli@ouce.ox.ac.uk

than one-third of the total precipitation variability. Furthermore, this method is unable to fully capture the evolving structure of dynamic systems such as the SACZ, especially on synoptic scales (Monahan et al. 2009). Another common approach in synoptic- and intraseasonal-scale analysis is to identify events through precipitation thresholds over an area of interest (Liebmman et al. 1999; Carvalho et al. 2002; Hirata and Grimm 2016; Mattingly and Mote 2017). This type of approach is effective in identifying events beyond the most common mode of variability but limits the analysis to events located over a specific region. Typically, past application of these methods focused only on the persistent SACZ events with little attention given to shorter-lived tropical–extratropical cloud bands.

In this study we present an automatic object-based methodology to identify cloud band events. Even though previous studies have proposed object-based cloud-tracking algorithms to identify SACZ events (Carvalho and Jones 2001; Carvalho et al. 2002, 2004; Rosa et al. 2020), built-in constraints on persistence and location have limited the extent of the selected events. The method proposed here, adapted from its application over southern Africa (Hart et al. 2012), is independent of the persistence and location of the cloud band, broadening the study of tropical–extratropical interactions beyond the SACZ and capturing the full spatiotemporal spectrum of synoptic-scale cloud band activity. The method allows stratification of SAm cloud bands by persistence, enabling identification of longer-lived SACZ events as one type of cloud band, as well as short-lived ones. This method underpins the first and second research questions this study addresses:

- How important are short-lived versus persistent cloud bands for the South American rainfall climatology?
- What atmospheric mean-state configurations support or reduce cloud band persistence?

The approach provides the necessary and long-needed sampling strategy to explore the interactions between synoptic- and seasonal-scale dynamics across the full spectrum of SAm cloud bands. During the SAm rainy season, cloud band and indeed SACZ activity results from the tropical convection over the Amazon (Figuroa et al. 1995; Gandu and Silva Dias 1998) interacting with the propagation of extratropical baroclinic waves through the subtropics (Nieto-Ferreira et al. 2011; van der Wiel et al. 2015; Rodrigues and Woollings 2017). The resultant tropical–extratropical connection provides the atmospheric instability necessary for the organization of the deep convection within the subtropical SACZ region (Ambrizzi and Ferraz 2015; Zanin and Satyamurty 2020). This convection, in turn, interacts with the basic state, altering the downstream propagation of the extratropical disturbances (van der Wiel et al. 2015; Hirata and Grimm 2016). Such an off-equatorial diabatic heating source can modify the mean flow and act as a Rossby wave (RW) source, as shown in previous season-scale studies (Sardeshmukh and Hoskins 1988; Shimizu and de Cavalcanti 2011; Rodrigues and Woollings 2017). The cloud band sampling methodology developed in this study provides an important synoptic-scale event set, which is used here to facilitate a comprehensive diagnosis of a third research question:

- How large a Rossby wave source is South American tropical–extratropical cloud bands?

Details about the data and methodology can be found in section 2. The cloud band events identified are compared to observed SACZ in section 3 while their location and precipitation characteristics are described in section 4. Section 5 explores the role of basic-state fluctuations on the development of cloud bands and section 6 explores the synoptic-scale circulation anomalies during the cloud band events as well as the effects of the enhanced subtropical convective activity in the local circulation. A discussion of the main results is presented in section 7, with their scientific relevance summarized in section 8.

2. Data and methodology

a. Datasets

The identification of cloud band events is based on the outgoing longwave radiation (OLR) version 1.2 dataset provided by the National Oceanic and Atmospheric Administration (NOAA) Climate Data Record (CDR) (Lee and NOAA-CDR Program 2011; Lee 2014) available from 1979 to the present. OLR data are estimated using high-resolution infrared radiation from low-Earth orbit satellite data, averaged to a daily temporal resolution on a 1° latitude–longitude grid.

Daily precipitation data are used to characterize the location and intensity of rainfall during events. Similar results were produced when using data from the fifth-generation reanalysis (ERA5) by the European Centre for Medium-Range Weather Forecasts (ECMWF; Hersbach et al. 2020), satellite-derived precipitation data from the Tropical Rainfall Measuring Mission version 3B42 V7 (TRMM; Huffman et al. 2014), and a gridded dataset based on station-observed precipitation from Brazil (Xavier et al. 2016). This analysis supported the use of ERA5 for the results presented here, chosen due to good spatial resolution ($\Delta x \sim 25$ km) and data availability for full period of OLR data (1979–2018).

The circulation characteristics of the cloud band events are derived from daily zonal (U) and meridional (V) wind at 200 and 850 hPa, also obtained from ERA5 reanalysis. Other circulation variables considered are divergent wind (∇_χ), divergence ($\nabla \cdot \mathbf{V}$), and absolute vorticity (η) and its gradient ($\nabla\eta$) at upper levels (200 hPa) and the zonally asymmetric streamfunction at 200 hPa (Ψ_{200}) and 850 hPa (Ψ_{850}). These derived variables are computed with the Python package *windspharm* (Dawson 2016), considering spherical harmonics truncated at total wavenumber 42.

b. Cloud band events: Identification and characterization

The basis of the proposed methodology is the identification of cloud band events through an automated detection algorithm developed by Hart et al. (2012, 2018). Using daily OLR data, the algorithm identifies contiguous areas with OLR below a threshold indicative of deep convective cloud (see example in Fig. 1; shading and pink contours represent an event identified on 12 January 2011). To be classified as a cloud band, areas of low OLR within the South American region (red

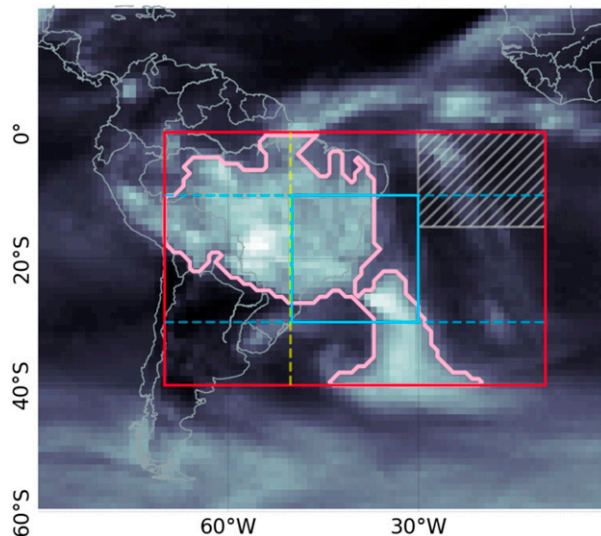


FIG. 1. Schematic of the study area: average OLR for 12 Jan 2011, representing a day with active cloud band event (shading; low OLR values in light shades), with the cloud band signature as identified by the algorithm (light pink contour). Other parameters utilized by the cloud band detection algorithm are the region of interest for cloud band occurrences (red square), the minimum latitudinal extension of the cloud bands (dashed blue lines), the area over which the cloud band should be diagonal (blue square), and the meridian defining the minimum eastern limit of the events (yellow dashed line). The OLR in the hatched area is excluded from the analysis.

square in Fig. 1) should extend from the tropics to the extratropics (i.e., from 10° to 30° ; dashed blue lines in Fig. 1) with bearing between -10° and -80° (rotated clockwise from true east) over eastern Brazil (EBr; blue square in Fig. 1). The bearing criterion can exclude events where the cloud band is connected to the Atlantic intertropical convergence zone, forming a large C-shaped structure over the study region. To avoid the exclusion of the subtropical extension of these cloud bands, we removed the OLR values east of 30°W and north of 15°S over the tropical Atlantic (hatched area in Fig. 1). Additionally, we guarantee that the events selected reach subtropical latitudes over the SATl by only considering cloud bands that have some extension eastward of 50°W (dashed yellow line in Fig. 1). This removes extensive cloud activity related to LLJ events that extend into SESA but does not necessarily extend into the SATl.

Key results are robust to the value of the OLR threshold, producing qualitatively similar event climatologies regardless of the number of days with cloud bands. For instance, we compared the results obtained considering a range of OLR thresholds to manually identified SACZ events noted in the operational forecast of the Centre for Weather Forecast and Climatic Studies (CPTEC; Centro de Previsão de Tempo e Estudos Climáticos) from the National Institute for Space Research (INPE; Instituto Nacional de Pesquisas Espaciais) [compiled by Rosso et al. (2018)]. The details of this comparison are described in section 3. The highest parity between the different approaches is obtained when using an OLR threshold of 225 W m^{-2} .

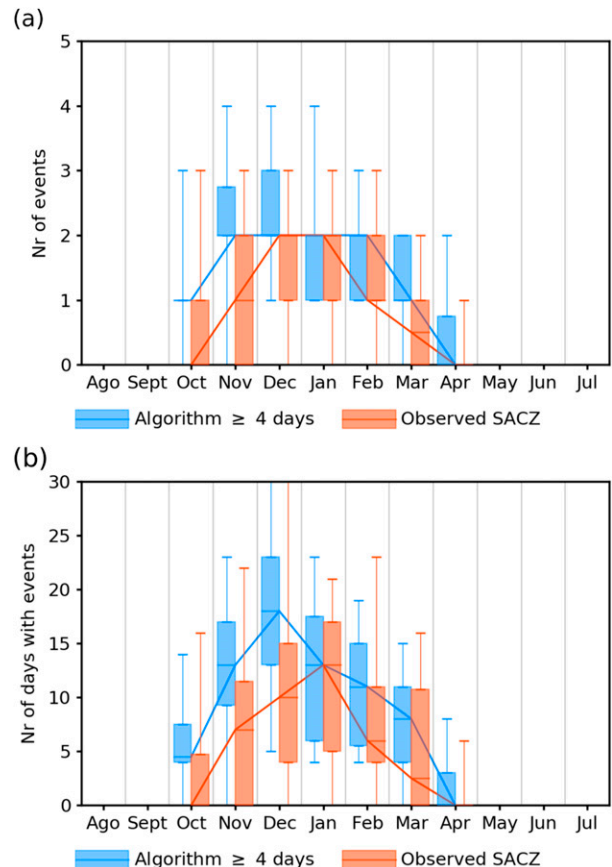


FIG. 2. Median (horizontal bars and solid lines), interquartile range (filled boxes), and minimum and maximum values (whiskers) for (a) number of events and (b) number of days with events considering observed SACZ [orange; data from Rosso et al. (2018)] and algorithm-detected events persisting for 4 or more days (blue).

The importance of cloud band events to the SAM regional climatology is characterized by their frequency, persistence, and volume of precipitation within the spatial signature of the cloud band. Precipitation, OLR, and circulation characteristics are estimated using composites of the days with events, averaged per month. All days within an individual event are averaged before estimating the monthly and seasonal mean, avoiding overrepresentation of the characteristics of more persistent events. The significance of the averages and anomalies are tested using the Student's t test (Wilks 2011a) with Hotelling's T^2 test (Wilks 2011b) applied to vector fields. In both cases, the null hypothesis (H_0) is that the averages (or anomalies) during the events are indistinct from the climatology. We analyzed all months in the 1979–2018 period, but we will focus on events occurring during the rainy season [November–March (NDJFM)] motivated by Fig. 2. Results are presented as the mean of the rainy season monthly averages or as the averages of individual months when necessary.

c. Analysis of subtropical Rossby wave dynamics

Cloud bands link the tropical latitudes to the extratropics. Thus, it is expected that these events will be under the influence

of forcings with tropical (through changes in the convection over the Amazon, for example) and extratropical origin, such as the propagation of Rossby waves. Here, we diagnose the subtropical RW dynamics by considering upper-level flow (200 hPa) over SAM. This part of the analysis is divided in two steps: first, we evaluate the role of the basic state in setting conditions favorable for RW propagation across subtropical SAM; second, we consider on the role of the resultant cloud bands, particularly when persistent, in creating feedback forcing onto the basic state.

In the first step, we evaluate how fluctuations in the basic flow interact with RW propagation across SAM, favoring the development of cloud band events on intraseasonal scales. This analysis is based on stationary RW propagation theory (Hoskins and Karoly 1981). We use this framework as a heuristic to evaluate how upper-level westerly flow changes influence the total wavenumber (K ; Hoskins and Karoly 1981; Hoskins and Ambrizzi 1993; Karoly 1983) and affect wave propagation into the SAM region. The value of K is calculated as shown:

$$K = \left(\frac{\beta_M}{\langle U_M \rangle - c_M} \right)^{1/2}, \quad (1)$$

where $\langle U_M \rangle$ is the monthly average of the zonal wind at 200 hPa, c_M is the zonal phase speed, and β_M is $\cos\phi$ times the meridional gradient of absolute vorticity and is defined as

$$\beta_M = \frac{2\Omega}{a} \cos^2\phi - \frac{d}{dy} \left[\frac{1}{\cos^2\phi} \frac{d}{dy} (\langle U_M \rangle \cos^2\phi) \right], \quad (2)$$

where a is the mean radius of Earth ($=6.37 \times 10^6$ m), Ω is its angular speed of rotation ($=7.292 \times 10^{-5}$ rad s $^{-1}$), and ϕ is the latitude. The formulation of Eq. (2) is for a Mercator projection, hence $\langle U_M \rangle = \langle U \rangle / \cos\phi$ and $c_M = c / \cos\phi$.

The term K defines the maximum wavenumber of a RW propagating with phase speed c through a basic state. For $c = 0$ m s $^{-1}$, Eq. (1) represents the maximum wavenumber of a stationary RW (K_S). Here, we adopt $c = 6$ m s $^{-1}$ to approximate the speed of the synoptic-scale RW propagation typically associated with cloud bands, following van der Wiel et al. (2015). According to Eq. (1), $K \rightarrow \infty$ when $(\langle U_M \rangle - c_M) \leq 0$, indicating that eastward propagating RW can only occur in areas with westerly winds ($\langle U \rangle - c > 0$). Furthermore, RW tend to refract toward areas with larger values of K , such as those with westerly winds over tropical eastern Pacific and western SATl, while areas with low K act as a barrier to the propagation of the waves. Consequently, areas of large K bounded by low- K regions, commonly found along the jet streams, are defined as waveguides trapping RW with a wavenumber larger than the low values of K (Hoskins and Karoly 1981; Hoskins and Ambrizzi 1993; Karoly 1983).

Strictly speaking, this theory is only valid for small perturbations about a basic state, which is arguable for large-amplitude RW in the subtropics. However, the theory provides a powerful heuristic for conceptualizing these waves (Wirth et al. 2018). Thus, we define periods of enhanced cloud band activity as those months with the monthly count of event days exceeding the 75th percentile. This approach yields on average

10 enhanced-activity months per month of the November to March season, from across the 1979–2018 period. The value of K is computed using the monthly zonal wind averages and enhanced cloud band activity maps of K are composited using the previously identified months. These results are interpreted as the average basic flow that strongly favors the propagation of RW necessary for the development of synoptic-scale cloud bands.

Given an environment favorable to the development of cloud bands, the second step focuses on understanding the effects of the enhanced subtropical convection from these events onto the basic flow, supporting their persistence as well as being a source of RW themselves. To diagnose the impact that the cloud band events may have on modifying the basic flow, we estimate the Rossby wave sources and sinks (RWS). As shown by Sardeshmukh and Hoskins (1988), regions with divergent winds, such as those occurring in areas with strong meridional gradients of zonal winds, can advect vorticity and act as a source of RW energy. Thus, the off-equatorial heating and upper-level divergence associated with cloud bands can act as a source of RW activity, locally modifying the environmental conditions and affecting the persistence of events.

Following Sardeshmukh and Hoskins (1988), the RWS can be estimated as follows:

$$\text{RWS} = -\nabla \cdot (\mathbf{V}_\chi \eta) = \underbrace{-\eta \nabla \cdot \mathbf{V}}_{S1} - \underbrace{\mathbf{V}_\chi \cdot \nabla \eta}_{S2}, \quad (3)$$

where \mathbf{V} is the wind, \mathbf{V}_χ its divergent component, and η the absolute vorticity. Utilizing a synoptic climatology approach made possible by our cloud band event set, we estimate the RWS for each event as perturbation RWS' around a basic state $\langle \text{RWS} \rangle$:

$$\text{RWS} = \langle \text{RWS} \rangle + \text{RWS}'. \quad (4)$$

Isolating RWS' in Eq. (4) and using the right-hand side of Eq. (3) yields

$$\text{RWS}' = [-\eta' \nabla \cdot \mathbf{V} - \mathbf{V}_\chi \cdot \nabla \eta] - [-\langle \eta \rangle \nabla \cdot \langle \mathbf{V} \rangle - \langle \mathbf{V}_\chi \rangle \cdot \nabla \langle \eta \rangle] \quad (5)$$

Now, considering the elements in the first and second terms of Eq. (5) also as a sum of perturbations (indicate with a prime) around a basic state (indicated with angle brackets), as in Qin and Robinson (1993), rearranging them and neglecting non-linear terms (products of perturbations), we get

$$\text{RWS}' = \underbrace{-\eta' \nabla \cdot \mathbf{V}}_{S1.1} - \underbrace{\langle \eta \rangle \nabla \cdot \mathbf{V}'}_{S1.2} - \underbrace{\mathbf{V}_\chi \cdot \nabla \eta'}_{S2.1} - \underbrace{\mathbf{V}_\chi' \cdot \nabla \langle \eta \rangle}_{S2.2}, \quad (6)$$

which is equivalent to the “WAVY LINEAR-C” model in Sardeshmukh and Hoskins (1988) [see also Eq. (2) in Qin and Robinson 1993]. In Eq. (6), the terms S1.1 and S1.2 represent the extratropical component of the RWS' and is driven mostly by the vortex stretching by the anomalous divergent flow [term S1.2 in Eq. (6)]. The terms S2.1 and S2.2 are the tropical component of the RWS', dominated by the advection of climatological absolute vorticity by the anomalous divergent

wind [term S2.2 in Eq. (6)] (Sardeshmukh and Hoskins 1988; Qin and Robinson 1993; Shimizu and de Cavalcanti 2011).

Here, (RWS) and RWS are estimated using daily data [as proposed in Qin and Robinson (1993)] for tropical–extratropical cloud bands, enabled by the event set created by our automatic cloud band identification. This analysis provides an indication of the extent to which individual cloud band events contribute to the climatological RW source identified in the SACZ region (Shimizu and de Cavalcanti 2011).

3. Comparison with observed SACZ events

The use of an automated detection algorithm can improve the identification of SACZ as well as short-lived cloud band events, without the constrictions of traditional event-selection methods. To demonstrate that the climatology and spatial OLR structure of the automatically detected events are similar to SACZ events, we compare these events to a manual record of SACZ (Rosso et al. 2018). This dataset—with observations from October to April and covering the period between December 1992 and February 2015—is from two main sources. Events occurring before 1996 were compiled by Rosso et al. (2018) from studies published in Brazilian conferences. After 1996, the events were identified by the CPTEC-INPE operational forecast and described in the Climanalise bulletin, published by INPE (Portuguese version available at <http://climanalise.cptec.inpe.br/~rclimanl/boletim/>).

To classify an SACZ event, CPTEC-INPE defined a set of dynamic and thermodynamic aspects based on the classical definition of a subtropical convergence zone from Kodama (1992, 1993) and on a previous study of the main SACZ characteristics (de Quadros 1994). A comprehensive description of the operational criteria can be found in Ambrizzi and Ferraz (2015) and Escobar (2019). Between 1992 and 2015, Rosso et al. (2018) identified 156 SACZ events, more frequent in December and January, with a median of two events per month (orange bars in Fig. 2a). The events lasted 1026 days in total (Table 1), with a median persistence of 6.6 days per event.

Considering only cloud bands lasting 4 or more days, in accordance with the observed SACZ criterion, the algorithm identified 237 events in a total of 1574 days (Table 1). By construction, the automated algorithm is only constrained by the location and extension of the cloud band in daily mean OLR, resulting in a larger number of events. Most of the extra days with cloud band events occurs in November, December, and February (Fig. 2b) and are located to the south of the observed SACZ (figure not shown). A similar bias is also detected by Rosa et al. (2020), who also compared the results obtained by an automatic-detection algorithm to this observed SACZ dataset. Nonetheless, the spatial OLR structure (figure not shown) and climatology (Fig. 2) of the automatically detected events is similar to the observed SACZ. On the other hand, the algorithm fails to identify part of the observed SACZ days (Table 1), characterized by events with little extratropical extension (figure not shown). Similar results are obtained when considering all cloud band events, regardless of their persistence, granted that the number of days with events is larger.

TABLE 1. Contingency table comparing the number of days with SACZ considering observed [data from Rosso et al. (2018)] and algorithm-detected events (only those persisting for 4 or more days). The marginal value indicates the sum over the column or row while frequency indicates the ratio between the marginal value and the total number of days considered (4881 days).

		Observed SACZ		Marginal	Frequency
		Yes	No		
Algorithm ≥ 4 days	Yes	681	893	1574	0.322
	No	345	2962	3307	0.678
Marginal		1026	3855	4881	1
Frequency		0.210	0.790	1	

4. Characteristics of cloud bands over South America

Between 1979 and 2018, the algorithm identified 4917 days with cloud bands, aggregated into 1761 events. Their seasonal cycle follows the typical precipitation cycle in the SAM monsoonal climate, with about 73.0% of the events occurring between October and March (Fig. 3a). Based on the results of section 3, cloud band events persisting 4 or more days (which will be referred to as persistent events) are a good proxy to identify SACZ events. Persistent events occur mainly between November and February (78.2% of the days with persistent events; Fig. 3b), with median of two events per month (Fig. 3a). They are present in 41.6% of the days of the rainy season (NDJFM) and contribute with more than one-third of the total precipitation, on average. Short duration events (i.e., those lasting up to 3 days thus excluding persistent ones, referred to as transient events from now on) prevail in the transition seasons, mainly in October, November, and March, with a median of four events per month. They occur in $\sim 18.2\%$ of the 151 days of the rainy season and contribute to $\sim 15\%$ of the total precipitation.

In addition to differences in their seasonal cycle, transient and persistent events also have different preferential locations during the rainy season. Persistent events extend over a large area of SAM with the associated precipitation forming a well-defined northwest–southeast-oriented band from the Amazon and extending across EBr toward western subtropical SATl (blue contours in Fig. 4, left column). Note that in Fig. 4, the total precipitation refers only to the precipitation within each cloud band signature, accumulated over all event days in the month. Over EBr and adjacent ocean, the persistent events are active in 20%–30% of the days in the rainy season (figure not shown) and are responsible for more than 50% of the monthly precipitation, especially in November to January (Figs. 4a,c,e). The average position of the persistent events migrates poleward from November on (Fig. 4a), reaching its southernmost position in February (Fig. 4g) and moving back equatorward in March (Fig. 4i). Both the spatial location and their fluctuations along the rainy season are similar to the observed SACZ events (Nielsen et al. 2019), further reinforcing the equivalence between persistent cloud band events identified automatically and SACZ events identified manually.

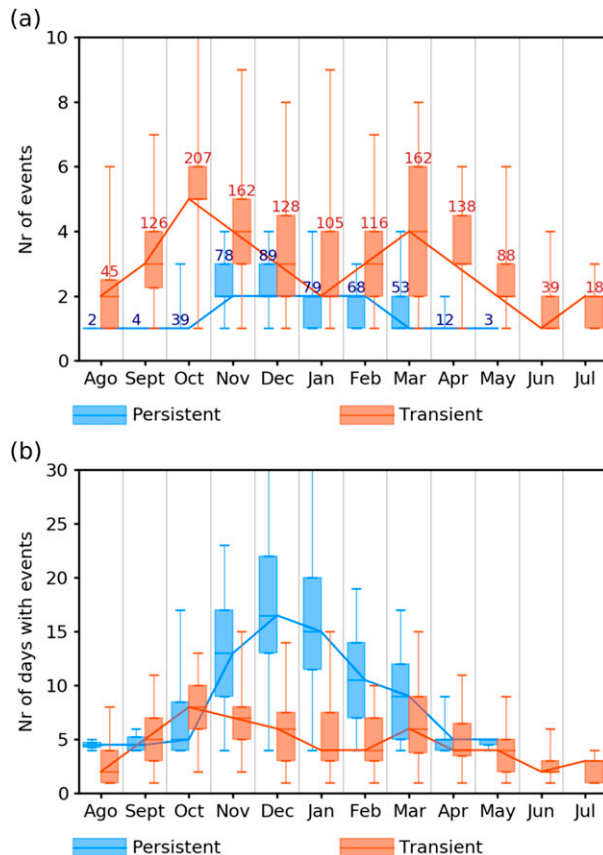


FIG. 3. Median (horizontal bars and solid lines), interquartile range (filled boxes), and minimum and maximum values (whiskers) for (a) number of events and (b) number of days with events, considering persistent (blue) and transient (orange) events. In (a), the number above each box represent the total number of events in each category (persistent and transient) per month.

Transient events are smaller, occurring preferentially over the continent and extending toward southern Brazil (red contours in Fig. 4, right column), with larger precipitation amounts over the Amazon (blue contours in Fig. 4, right column). These events are active, on average, in 4%–14% of the 151 days of the rainy season (figure not shown) and contribute up to 20% of the total climatology (shading in Fig. 4, right column). This contribution is larger along the margins of the dominant SACZ rainfall band (shading in Fig. 4, right column), highlighting the importance of cloud bands in fulfilling the expected climatology outside the spatial signature of the SACZ. In November and December, transient events also make a substantial contribution to the rainfall climatology over SESA (Figs. 4b,d).

5. Role of variations in the basic state on cloud band activity

As a first step to understand differences in the location and duration of the events, we analyze the preconditioning of the basic state as an envelope to the cloud band activity. Considering months with enhanced transient and persistent

cloud band activity (as described in section 2c), we analyzed the maximum wavenumber (K) associated with typical synoptic-scale RW propagating with phase speeds of $c = 6 \text{ m s}^{-1}$ (Hoskins and Karoly 1981; van der Wiel et al. 2015).

During the rainy season, the circulation over SAM is characterized by an area of minimum K at $\sim 40^\circ\text{S}$ (shading in Fig. 5b), located at the core of the subtropical jet (black contour at Fig. 5b) and flanked by two RW guides. Longer RW (wavenumber below 6) are able to propagate from the mid-latitudes toward South America while shorter waves are restricted to the latitudinal band north or south of the minimum K . In the subtropics, the large gradient of K —a result of anticyclonic meridional shear at the equatorward flank of the subtropical jet—forces an anticyclonic curvature on the RW propagation rays, deflecting them equatorward. Previous studies identified similar waveguide characteristics during austral summer over SAM (Hoskins and Ambrizzi 1993; van der Wiel et al. 2015).

In months with enhanced activity of persistent cloud band events, the presence of westerly anomalies north of 30°S (blue lines on the right side of Fig. 5a) locally reduces the value of K by $\sim 10\%$ over EBr coast (Fig. 5a). During these months, the critical line ($u = c = 6 \text{ m s}^{-1}$) is located to the north of its climatological position over EBr (black contours in Figs. 5b,c), favoring the propagation of RW deeper into the tropics. Slower RW (i.e., those with smaller phase speed) are even more strongly influenced by the westerly anomalies over these latitudes (Fig. 5a). Since persistent events represent 42% of the days in the rainy season on average, their composite is similar to the climatology, highlighting the importance of these events in determining the basic state over SAM.

In months with enhanced activity of transient events, the presence of easterly anomalies near 20°S (thin red lines in Fig. 5a) shifts the critical line poleward (black contours in Fig. 5d), resulting in an increase of K north of 25°S (thick red lines in Fig. 5a). This shift of the critical line blocks lower-latitude propagation of RW. South of 40°S , the westerly winds are enhanced (red lines to the right of Fig. 5a), extending the subtropical jet (STJ) toward SAM (black contours in Fig. 5d). These anomalies increase the meridional wind shear over the northern flank of the jet, which result in a larger extratropical–tropical gradient of K and consequently a larger anticyclonic curvature of the ray paths for RW propagation toward the tropics. The tightening of the gradient of K also favors the anticyclonic wave breaking (Woollings et al. 2018) and the development of blocking events over the region (Rodrigues and Woollings 2017). These results apply irrespective of RW phase speed (red lines in Fig. 5a).

6. Synoptic-scale analysis

a. Circulation characteristics during cloud band events

1) PERSISTENT EVENTS

During persistent events, the upper-level circulation (200 hPa) is characterized by cyclonic anomalies over southern Brazil (Ψ_{200} ; contours in Fig. 6a), limiting the Bolivian high (BH; arrows in Fig. 6a). These anomalies occur within an

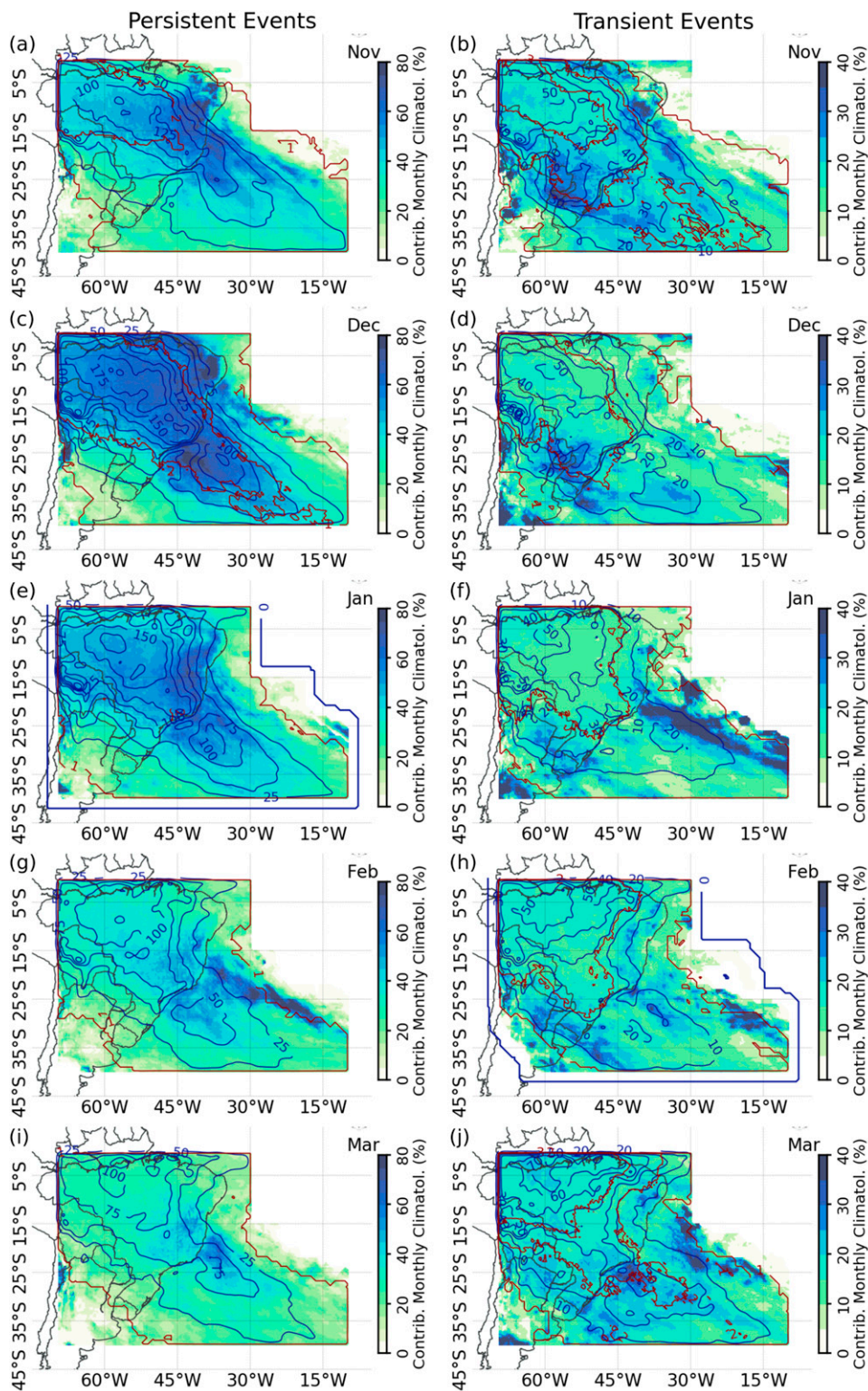


FIG. 4. Number of events (red contours), total precipitation during events (blue contours, every 25 mm month⁻¹ for persistent events and every 10 mm month⁻¹ for transient events), and contribution to the monthly climatology (shading; in %) averaged per month for (left) persistent and (right) transient events considering the ERA5 dataset. Note the different scales between the columns.

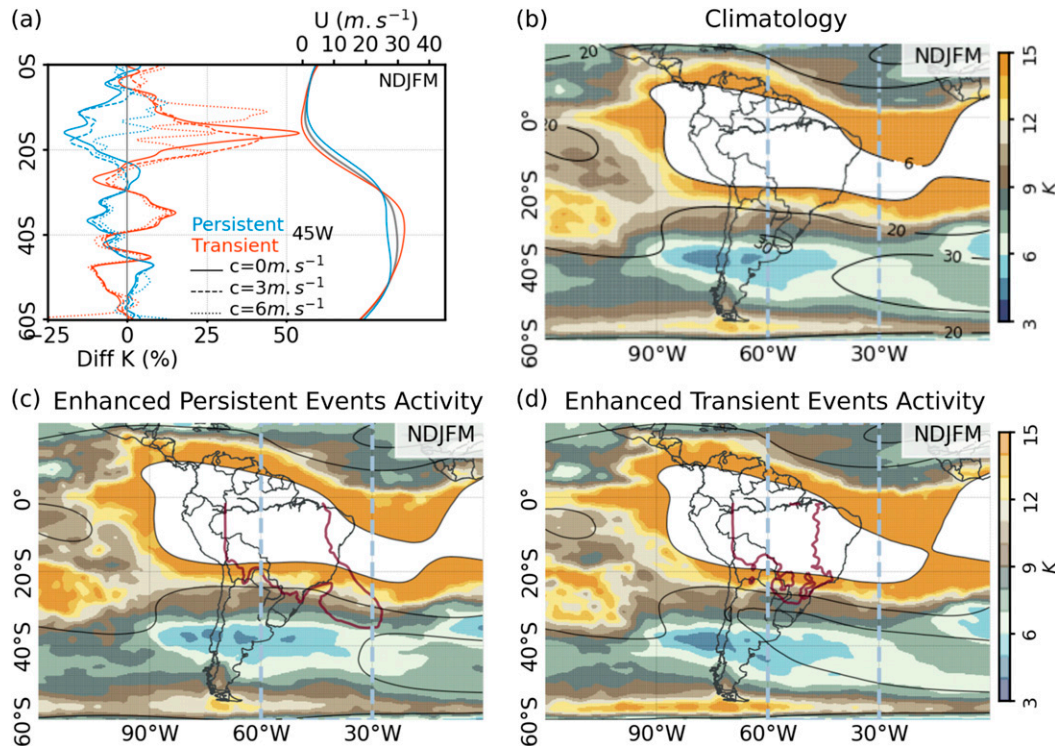


FIG. 5. (a) Percentage difference of the seasonal average of the latitudinal profile of K during months with enhanced persistent (blue lines) and transient (red lines) event activity in comparison to the climatological average, considering values of phase speed c of 0, 3, and 6 m s^{-1} (solid, dashed, and dotted lines, respectively). Values are zonally averaged between 60° and 30°W at 200 hPa [dashed gray rectangle in (b)–(d)]. (b)–(d) K (shading; in m s^{-1}) and zonal wind [contours at 6 ($u - c = 0$), 30, and 40 m s^{-1}] at 200 hPa averaged over the rainy season (NDJFM), considering the (b) climatology and months with enhanced activity of (c) persistent and (d) transient cloud band events. Areas with $u - c \leq 0$ are masked out. The purple contour delimits the area of events with accumulated precipitation above 50 mm month^{-1} in (c) and 30 mm month^{-1} in (d).

anomalous trough on the STJ (shading in Fig. 6a), which brings areas of westerly winds deeper into tropical latitudes, locally increasing the anticyclonic meridional shear of the zonal wind. The positive advection of vorticity along the northern flank of the upper-level cyclonic anomalies triggers rising motion, resulting in enhanced convection and upper-level divergence along the cloud band. The reduced area where the null hypothesis (H_0) can be rejected, especially in December and January (Figs. 7e,h), indicates the importance of these events in defining the climatology of the region. During these months, persistent cloud band events occur in 54.8% and 50.3% of the days, respectively. In the midlatitudes, areas of anticyclonic anomalies are observed upstream and downstream from the cyclonic anomalies, forming a RW propagating from southeastern Pacific (contours in Fig. 6a) toward southern Brazil and zonally crossing the SATl toward the African continent, albeit with reduced intensity (see also Fig. 7, center column). This behavior is more evident in November to January (Figs. 7b,e,h). These anomalies are typical of SACZ events (Kodama 1992, 1993; Lenters and Cook 1997; Liebmann et al. 1999; Carvalho et al. 2004, 2011; Gonzalez and Vera 2014) and resemble the “onset cold fronts” observed during and after the onset of

the South American monsoon system (SAMS) over EBr (see Nieto-Ferreira et al. 2011).

The upper-level circulation anomalies favor the establishment of lower level (850 hPa) cyclonic anomalies (Ψ_{850} ; contours in Fig. 6c) and associated low pressure system, forming a baroclinic structure centered over southeastern Brazil (SEBr). The anomalous southerlies over the west flank of the cyclonic anomalies (shading in Fig. 6c) weaken the LLJ, reducing the moisture transport from the Amazon toward SESA. Instead, the moisture is advected into the cloud band by the westerly anomalies along the northern flank of the low (arrows in Fig. 6c). Over subtropical SATl, the lower-level circulation is characterized by anticyclonic anomalies at $\sim 35^\circ\text{S}$, 15°W (contours in Fig. 6c; see also Fig. 8, center column), suggesting a deepening of the South Atlantic subtropical high (SASH). Together with the cyclonic anomalies over the continent, these anomalies increase the pressure gradient (Fig. 8, center column), accelerating the poleward flow over western subtropical SATl (arrows in Fig. 6c) and further contributing to the moisture advection into the cloud band. The mass convergence formed by the westerly anomalies from the Amazon advecting humidity into EBr and northerly anomalies around the western periphery of the SASH defines the

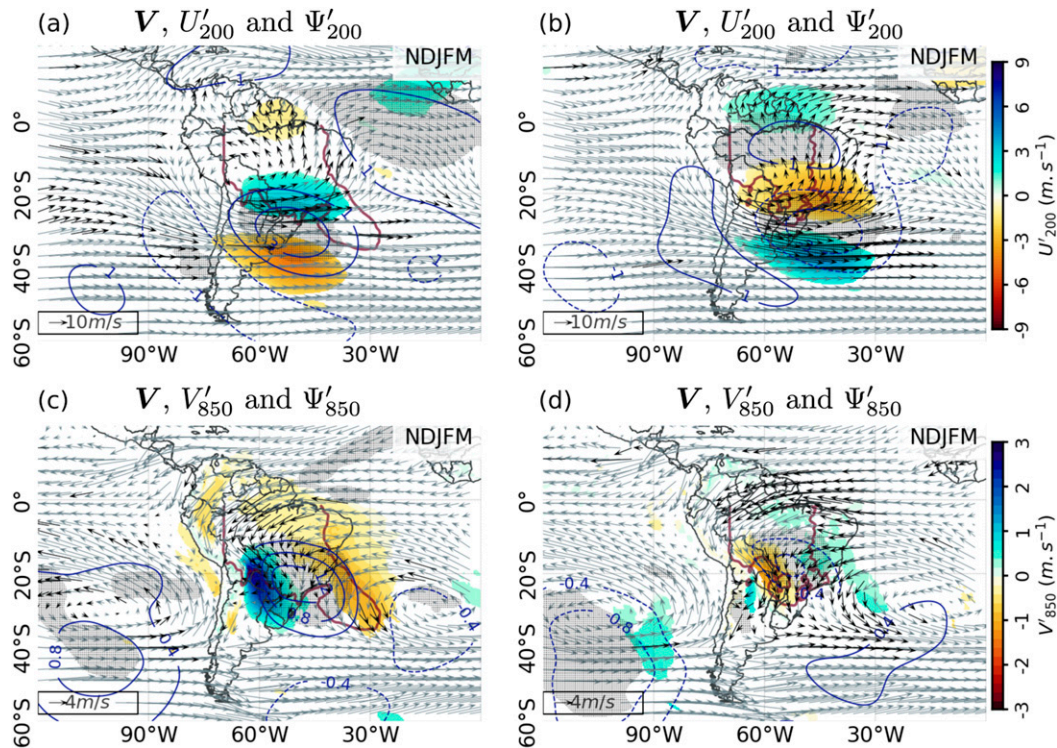


FIG. 6. Rainy season (NDJFM) circulation during (left) persistent and (right) transient events: (a),(b) average 200-hPa wind field (arrows; in m s^{-1}), U'_{200} (shading; in m s^{-1}), and Ψ'_{200} anomalies (contours, every $2 \times 10^6 \text{ m}^2 \text{ s}^{-1}$); (c),(d) average 850-hPa wind field (arrows, in m s^{-1}), V'_{850} (shading; in m s^{-1}), and Ψ'_{850} anomalies (contours, every $0.4 \times 10^6 \text{ m}^2 \text{ s}^{-1}$). In all panels, the zero contours are omitted and negative ones are dashed; the purple contour delimits the area of events with accumulated precipitation above (left) 50 and (right) 30 mm month^{-1} . Significant values ($p \leq 0.05$ in at least 2 of the 5 months) of vector fields during events are plotted as black arrows; gray shading highlights where contour fields are significant; and color-shaded fields only shown where significant.

SACZ activity (Nogués-Paegle and Mo 1997; Kodama 1992, 1993; Ambrizzi and Ferraz 2015).

2) TRANSIENT EVENTS

In general, the circulation anomalies during transient events are opposite to those during persistent events. In upper levels (200 hPa), anticyclonic anomalies over SESA and subtropical southwestern SATl (Ψ'_{200} ; contours in Fig. 6b) indicate an east/southeastward expansion of the BH (see also Fig. 7, right column), extending the area of easterly winds into subtropical latitudes (shading in Fig. 6b). On the other hand, the westerly anomalies over the south flank of the anticyclone indicate an acceleration of the STJ. This configuration increases in the wind shear and favors the anticyclonic RW breaking over the region, leading to the development of blocking events as described by Rodrigues and Woollings (2017).

Northwestward and southwestward of the upper-level anticyclonic anomalies, a pair of cyclonic anomalies (Ψ'_{200} ; contours in Fig. 6b) show that transient events are also associated with RW propagation. In November, the RW is practically zonal, crossing SAM at $\sim 30^\circ\text{S}$ and propagating toward Africa (contours in Fig. 7c). In December, the anticyclonic anomalies over eastern Pacific migrate poleward and the RW develops an

equatorward curvature as it progresses toward the SATl (Fig. 7f). From January on, the anticyclonic anomalies over eastern Pacific are farther poleward and the RW anticyclonic curvature is larger; however, the RW does not propagate eastward across the SATl (Figs. 7i,j,o).

In lower levels (850 hPa), transient events are characterized by anticyclonic circulation anomalies over central Brazil (Fig. 6d), indicating an expansion of the SASH toward the continent. This configuration is often characterized as an atmospheric blocking, which hinders the formation of SACZ and has been linked to the recent drought observed over SEBr (Coelho et al. 2016a,b; Rodrigues and Woollings 2017; Rodrigues et al. 2019). Furthermore, the anticyclonic anomalies accelerate the easterly winds over the EBr coast, increasing the advection of relatively drier air from the tropical SATl and inhibiting convection and precipitation over the region (Lintner and Neelin 2010). Over the western flank of the anticyclonic anomalies, the acceleration of the northerly winds indicates an enhancement of the LLJ (contours and shading, respectively, in Fig. 6d). This configuration favors the advection of moisture from the Amazon toward SESA, enhancing the precipitation. The resulting areas of anomalous ascending motion and upper-level divergence (Fig. 6d) provide an environment favorable to the development of

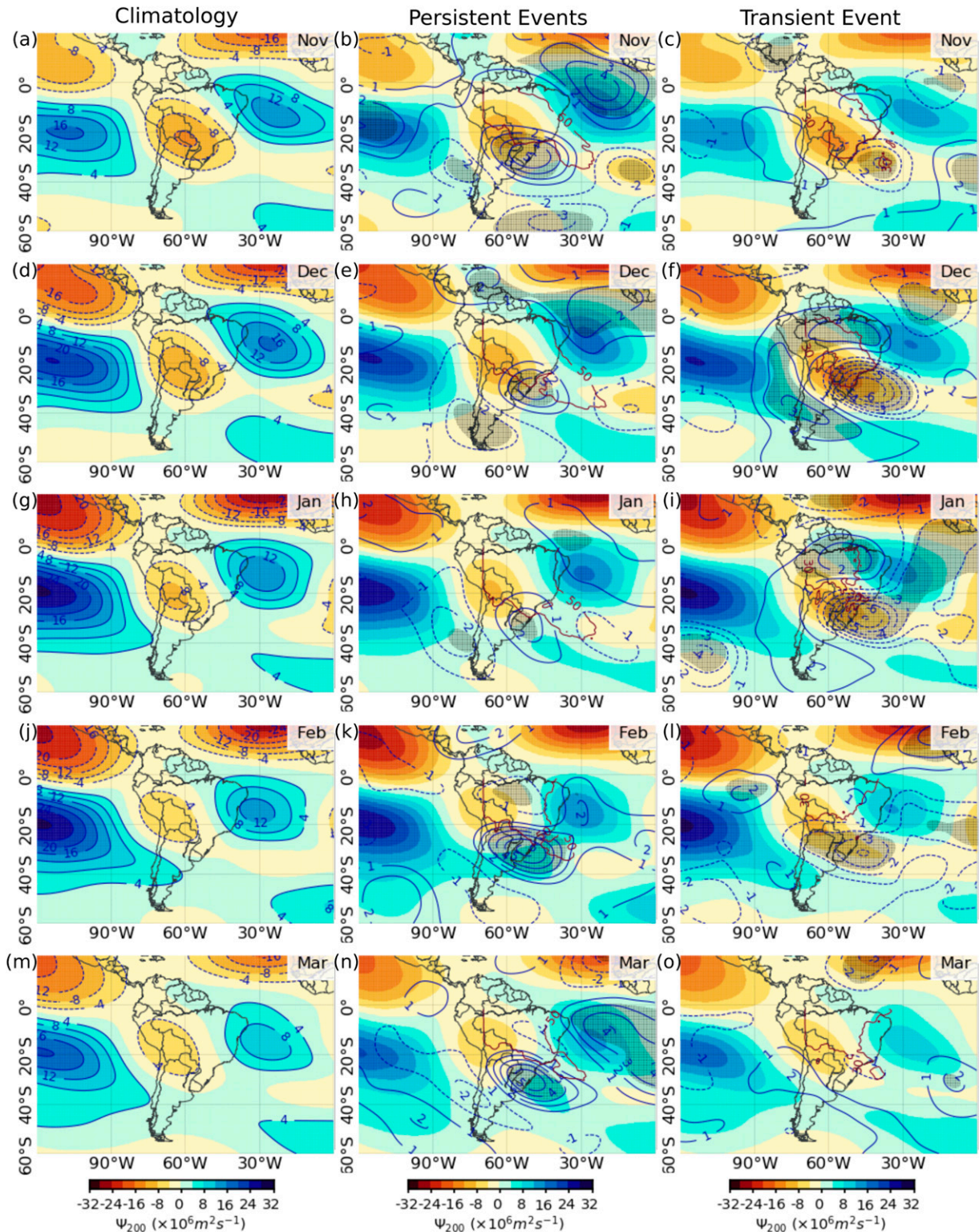


FIG. 7. Zonally asymmetric Ψ_{200} at 200 hPa. (left) Monthly climatology (shading and contours every $4 \times 10^6 \text{ m}^2 \text{ s}^{-1}$, negative dashed and zero omitted). (center), (right) Average (shading, in $\times 10^6 \text{ m}^2 \text{ s}^{-1}$) and anomalies (contours every $1 \times 10^6 \text{ m}^2 \text{ s}^{-1}$, negative dashed and zero omitted) during persistent and transient events, respectively. The purple contour delimits the area of events with accumulated precipitation above (center) 50 and (right) 30 mm month^{-1} . Areas with significant anomalies ($p \leq 0.05$) are shaded in gray.

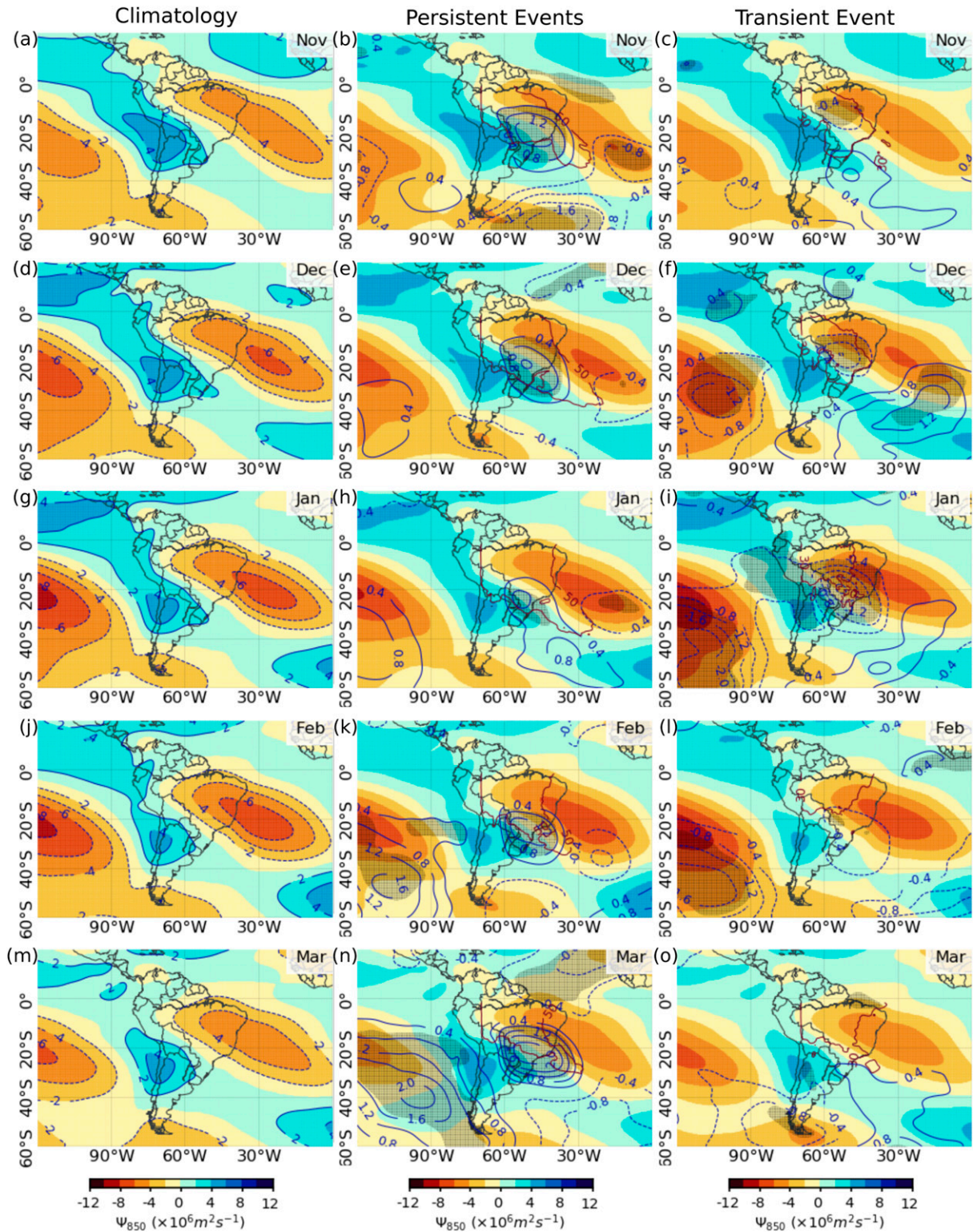


FIG. 8. Zonally asymmetric Ψ_{850} at 850 hPa. (left) Monthly climatology (shading and contours every $2 \times 10^6 \text{ m}^2 \text{ s}^{-1}$; negative dashed and zero omitted). (center),(right) Average (shading; in $\times 10^6 \text{ m}^2 \text{ s}^{-1}$) and anomalies (contours every $0.4 \times 10^6 \text{ m}^2 \text{ s}^{-1}$, negative dashed and zero omitted) during persistent and transient events, respectively. The purple contour delimits the area of events with accumulated precipitation above (center) 50 and (right) 30 mm month⁻¹. Areas with significant anomalies ($p \leq 0.05$) are shaded in gray.

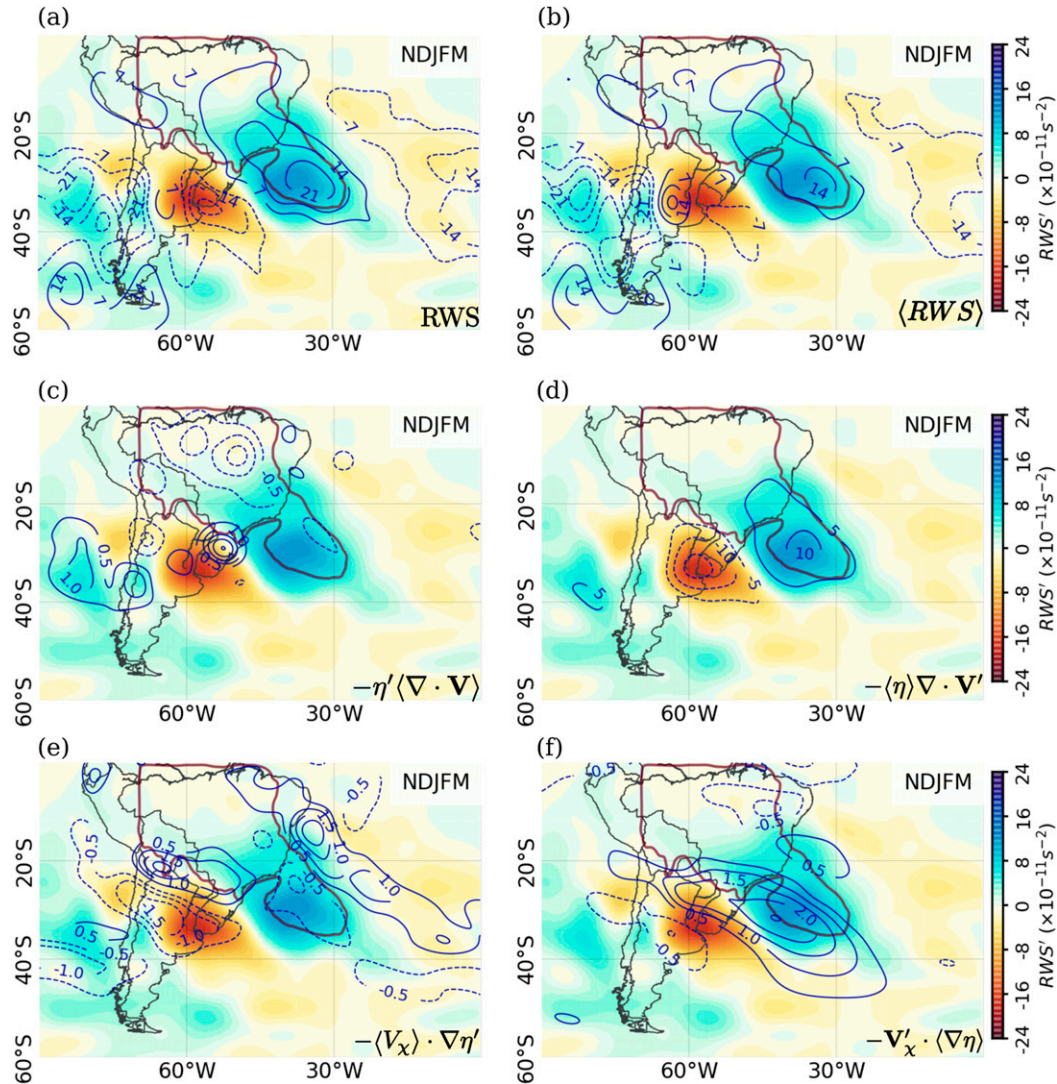


FIG. 9. Rainy season average (NDJFM) for RWS' (shading; in $\times 10^{-11} \text{ s}^{-2}$), (a) RWS [estimated by Eq. (4); contours every $7 \times 10^{-11} \text{ s}^{-2}$], (b) $\langle RWS \rangle$ (contours every $7 \times 10^{-11} \text{ s}^{-2}$), and each of the terms in Eq. (6): (c) $S1.1 = -\eta' \langle \nabla \cdot \mathbf{V} \rangle$ (contours every $0.5 \times 10^{-11} \text{ s}^{-2}$), (d) $S1.2 = -\langle \eta \rangle \nabla \cdot \mathbf{V}'$ (contours every $0.5 \times 10^{-11} \text{ s}^{-2}$), (e) $S2.1 = -\langle \mathbf{V}_x \rangle \cdot \nabla \eta'$ (contours every $0.5 \times 10^{-11} \text{ s}^{-2}$), and (f) $S2.2 = -\mathbf{V}'_x \cdot \langle \nabla \eta \rangle$ (contours every $0.5 \times 10^{-11} \text{ s}^{-2}$). In all maps, negative values are represented as dashed contours, with zero omitted. Purple contour delimits the area of events with accumulated precipitation above 50 mm month^{-1} .

mesoscale convective systems that are well documented in this area (Vera et al. 2006; Mattingly and Mote 2017).

b. Rossby wave sources and sinks

The previous section (section 6a) documented how RW associated with persistent events have a large signature across subtropical Brazil and into the SATl while those associated with transient events are confined more poleward. To diagnose the potential of these events to influence downstream RW propagation we analyze the Rossby wave sources and sinks (RWS), according to Eq. (4), with its anomalies (RWS') estimated using Eq. (6). Each of the terms in Eq. (6) is estimated separately and are represented as the contours in Figs. 9c–f (persistent

events) and Figs. 11c–f (transient events). The RWS' , which is the sum of these terms, is represented as shading in these figures. For reference, we have included the $\langle RWS \rangle$ as contours in Figs. 9b and 11b. The sum of these terms results in RWS [according to Eq. (4)], represented in Fig. 9a (persistent) and Fig. 11a (transient).

During persistent events, areas of positive RWS' are located in the oceanic portion of the cloud bands (shading in Fig. 9), reinforcing the large values of $\langle RWS \rangle$ observed in the climatology (Fig. 9b; see also Shimizu and de Cavalcanti 2011). Shimizu and de Cavalcanti (2011) show that both terms in Eq. (3) contribute to the large values of $\langle RWS \rangle$ over EBr (contours in Fig. 9b). The resulting large values of RWS over

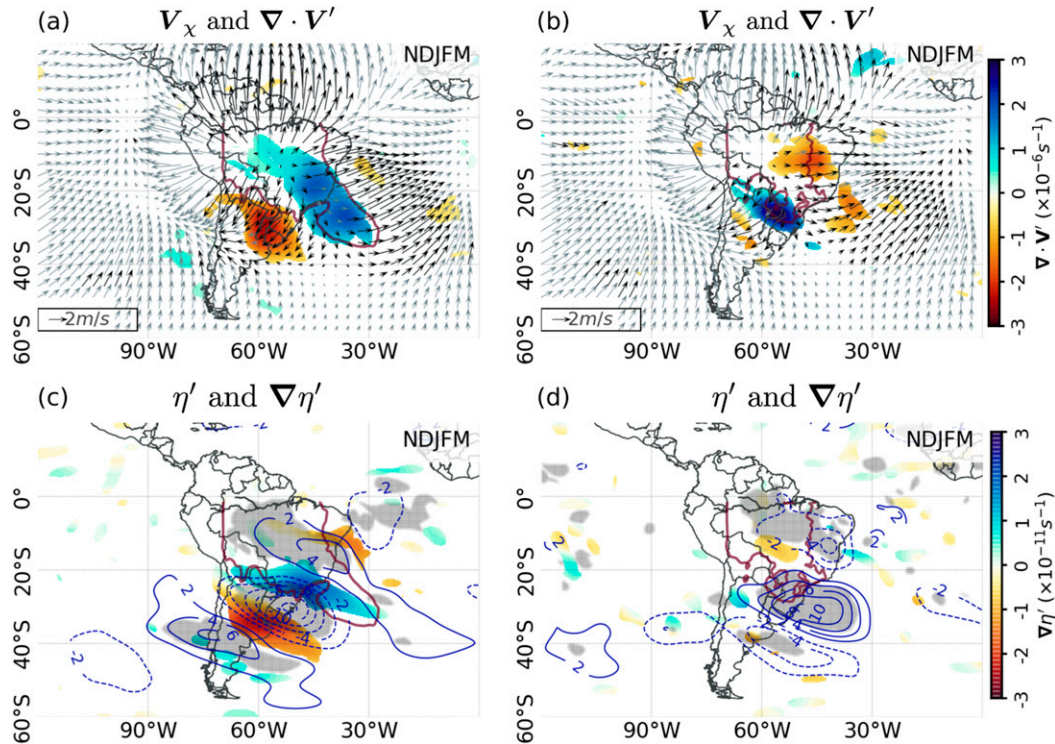


FIG. 10. Rainy season (NDJFM) upper-level (200 hPa) circulation during (left) persistent and (right) transient events: (a),(b) average divergent wind field (V'_x , arrows; in m s^{-1}) and divergence anomalies ($\nabla \cdot V'$; shading, in $\times 10^6 \text{ s}^{-1}$); (c),(d) anomalies of absolute vorticity (η' , shading; in $\times 10^6 \text{ s}^{-1}$) and its gradient ($\nabla \eta'$; contours every $2 \times 10^{-11} \text{ s}^{-1}$). In all panels, the zero contours are omitted and negative ones are dashed; the purple contour delimits the area of events with accumulated precipitation above (left) 50 and (right) 30 mm month^{-1} . Significant values ($p \leq 0.05$ in at least 2 of the 5 months) of vector fields during events are plotted as black arrows; gray shading highlights where contour fields are significant; and color-shaded fields only shown where significant.

the cloud band signature (Fig. 9a) could influence the development of the anticyclonic anomalies observed over central SATl, as suggested in previous studies, both for synoptic (Grimm and Silva Dias 1995; Grimm and Reason 2015; Rodrigues and Woollings 2017) and intraseasonal SACZ variability (Gonzalez and Vera 2014; Vera et al. 2018).

During persistent events, RWS' (shading in Fig. 9) is driven mostly by vortex stretching due to anomalous upper-level divergence [S1.2 in Eq. (6); contours in Fig. 9d; note the larger interval between contours for this term]. This result is expected since the presence of upper-level divergence related to convective activity is the most common source of RW in subtropical latitudes (Qin and Robinson 1993; Shimizu and de Cavalcanti 2011).

Locally, the advection of average vorticity by the anomalous divergent wind [S2.2 term in Eq. (6)] enhances (offsets) the positive (negative) values of RWS' along (south of) the poleward margin of the cloud band spatial signature (contours in Fig. 9f). Positive values of S2.2 are driven by the north/northeasterly divergent winds emanating from the cloud band convection (arrows in Fig. 10a) and interacting with areas of large gradients of mean vorticity along the equatorward flank of the STJ [figure not shown; climatological vorticity and its gradient can be found in Shimizu and de Cavalcanti (2011), their Fig. 3]. This term is

stronger in November, February, and March (figure not shown) due to the seasonal migration of the STJ, which increases the magnitude of vorticity gradient, similar to what is observed in the climatology (Shimizu and de Cavalcanti 2011).

Along the equatorward margin of the cloud band, the anomalous gradient of vorticity due to the deep convection is advected by the west/southwesterly divergent winds [S2.1 in Eq. (6); contours in Fig. 9e], delimiting the tropical boundary of the positive RWS'. The anomalies in the vorticity gradient over this region are related to the deepening of the Nordeste low (contours in Fig. 7, center column), considered one of the characteristics of the SACZ events (Carvalho et al. 2004; Ambrizzi and Ferraz 2015), and associated with enhanced precipitation over the continental SACZ (Mattingly and Mote 2017). Finally, the values of the anomalous vortex deformation by the divergence [S1.1 in Eq. (6); contours in Fig. 9c] are small and localized mainly over the Amazon, not substantially contributing to RWS' and consequently neither to RWS.

The anticyclonic vorticity tendency (positive RWS) induced by the enhanced convection (contours in Fig. 9a) is ahead of the cyclonic anomalies associated with the propagating RW (contours in Fig. 6b; see also the negative vorticity anomalies in Fig. 10c), weakening the wave. This is opposite to tendencies described by van der Wiel et al. (2015) and will be discussed in

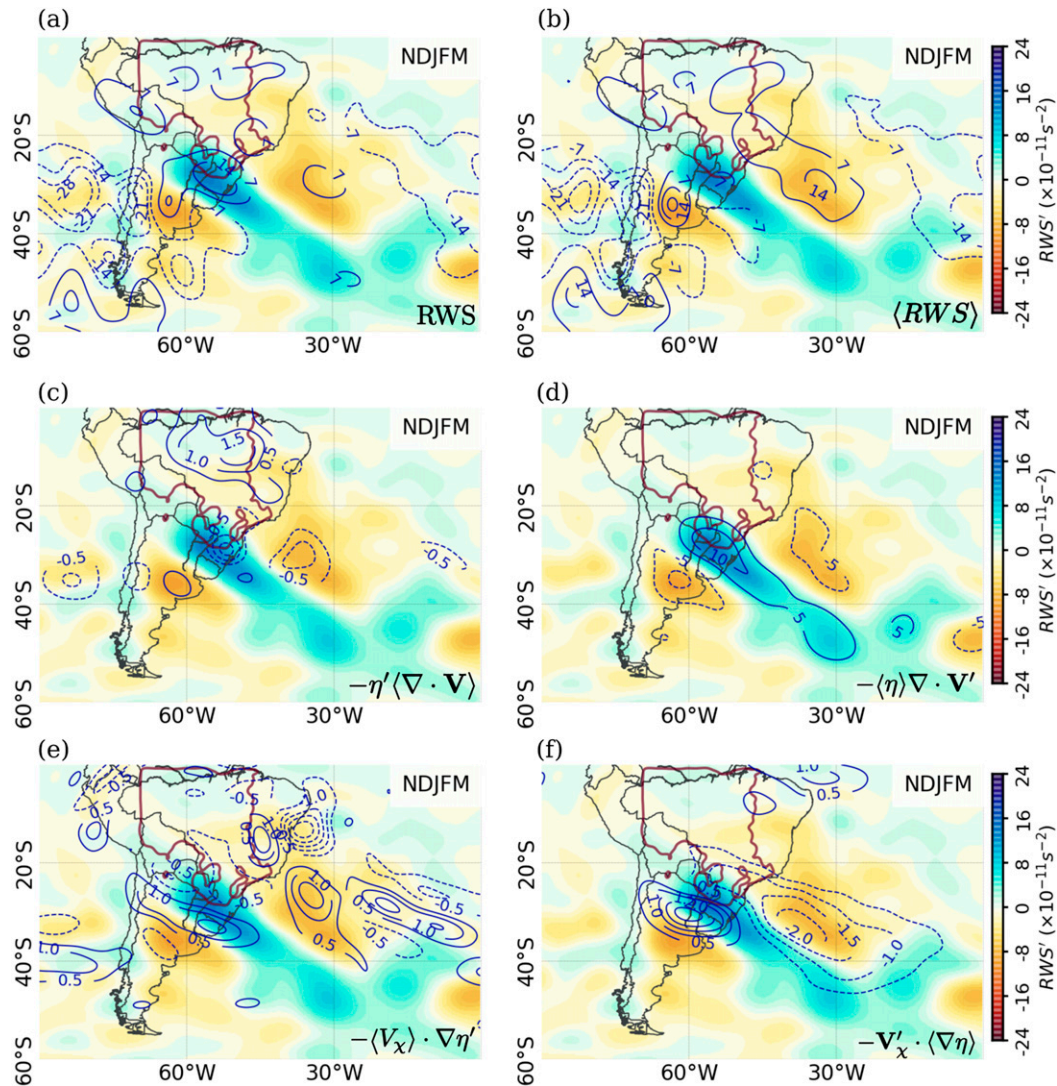


FIG. 11. As in Fig. 9, but for transient events. The purple contour delimits the area of events with accumulated precipitation above 30 mm month^{-1} .

section 7. On the other hand, the anticyclonic vorticity tendency is a source of RW on itself, contributing to the downstream anticyclonic anomalies over central SATl ($\sim 35^\circ\text{S}$, 15°W).

During transient events, areas with positive RWS and RWS' (contours and shading in Fig. 11a, respectively) occur over southern Brazil and SESA while negative ones are observed northeastward and southwestward. The negative RWS' over subtropical SATl (shading in Fig. 11) are strong enough to offset the positive (RWS) (contours in Fig. 11b), resulting in $RWS \sim 0$ over the region (Fig. 11a). As before, the RWS' is driven mainly by vortex stretching by the divergence anomalies [S1.2 in Eq. (6); Fig. 11d]. Positive values of S1.2 are located at the upper-level divergence resulting from the enhanced convection over southern Brazil (Fig. 10b) and extend over western subtropical SATl. Despite the weaker convection during transient events, its location south of 20°S , where $\langle \eta \rangle$ is large, results in large values of S1.2.

The areas of negative S1.2 on both sides of the positive ones are driven by the resulting convergence and compensatory subsidence (Fig. 10b) and reinforced by the west- and southwesterly advection of vorticity gradient by anomalous divergent wind (Fig. 10b) emanating from the subtropical convection [S2.2 in Eq. (6); Fig. 11f]. This term is more relevant during summer (figure not shown) due to the large gradient of vorticity associated with the seasonal migration of the STJ, as observed by Shimizu and de Cavalcanti (2011).

Anomalies of vorticity and its gradient caused by the RW propagation are advected by the mean divergent wind resulting in locally strong values of S2.1 (Fig. 11e) that offset the negative value of RWS' over western SATl. However, the seasonal average of S2.1 is small due to the large variation in the position of the anticyclonic circulation anomalies throughout the rainy season. The contribution of the terms associated with

anomalous vortex deformation [S1.1 in Eq. (6)] are small and concentrated over the Amazon (Fig. 11c).

Thus, during transient events, the anticyclonic vorticity tendency resulting from the subtropical convection (Fig. 11a) is weaker and located within the anticyclonic vorticity, characteristic of the RW propagation (Fig. 10b). The interaction between the anomalous divergent winds and the strong mean vorticity gradient along the equatorward flank of the STJ result in cyclonic vorticity tendencies over western SATl that block the downstream propagation of the RW. This pattern is coherent with blocking events resulting from RW breaking over SAM described by [Rodrigues and Woollings \(2017\)](#). Opposite to persistent events, the anticyclonic vorticity tendencies resulting from the transient events are not strong enough to act as a RW source and minimal downstream propagation of the midlatitude disturbances is likely.

7. Discussion

The flexibility of the detection algorithm allows the tracking of cloud band events responsible for almost 60% of the region-wide precipitation during the rainy season (up to 80% locally). Stratifying these events by their persistence is a straightforward way to identify the SACZ events as those lasting 4 or more days. These events contribute the majority of the total rainy season precipitation over SEBr, despite being active in less than 30% of the days (151 days per rainy season). Additionally, the approach also emphasizes the relevance of transient events to the climatology. Despite being active only ~10% of NDJFM days, these events contribute to ~15% of the total precipitation, especially over SESA. Persistent and transient events have distinct location, strongly mapping onto the SACZ-related dipole ([Carvalho et al. 2004, 2011](#); [Gonzalez and Vera 2014](#)): persistent events occur mostly over EBr while transient events are preferentially located over SESA. This stratification by persistence proved particularly fruitful for diagnosing differences in RW dynamics associated with cloud bands over SAM.

a. Persistent events

Figure 12 presents a conceptual summary of these findings. During the rainy season, cloud bands are related to the equatorward propagation of extratropical disturbances, with zonal wind anomalies in the basic state modulating the RW propagation over SAM and consequent location of the convective activity. In months with enhanced persistent events activity, westerly winds over eastern tropical SAM shifts the RW critical line equatorward (black dotted lines in Fig. 12a, top) allowing deeper incursions of the upper-level disturbances into tropical latitudes (thick green line in Fig. 12a, top). The sharpening of the meridional gradient of zonal wind near 20° (dotted gray lines in Fig. 12a, top) results in an environment favorable for the development of backward-tilting troughs with potential for cutoff low development ([Thorncroft et al. 1993](#)). During the onset of the rainy season, the midlatitude upper-level jet weakens and migrates poleward, increasing the anticyclonic shear between 20° and 30° and supporting the development

of stationary cold fronts over the region ([Nieto-Ferreira et al. 2011](#)).

On synoptic scales, persistent events occur when RW propagating equatorward along eastern SAM coast reach tropical latitudes. The advection of cyclonic vorticity ahead of the upper-level cyclonic anomalies induces upward movement, triggering deep convection and upper-level divergence over EBr and adjacent SATl (blue spiral in Fig. 12a, bottom). This enhanced convection, in turn, produces northeasterly divergent winds over SESA (arrows in Fig. 12a, bottom) and interacts with the local (negative) vorticity and its gradient, favoring convergence over the region (yellow spiral in Fig. 12a, bottom). This pattern is coherent with the active phase of the SACZ dipole ([Nogués-Paegle and Mo 1997](#); [Grimm and Zilli 2009](#); [Gonzalez and Vera 2014](#)), with the compensatory subsidence reinforcing the STJ trough, as shown in simulations performed by [Figueroa et al. \(1995\)](#) and [Gandu and Silva Dias \(1998\)](#).

While the propagation of RW and development of cloud bands may be supported by a necessary basic state, the cloud bands modify the local and regional circulation and therefore this basic state. The anticyclonic vorticity tendency induced by the enhanced convection counteracts the cyclonic circulation anomalies, slowing down RW propagation (thick green line in Fig. 12a, top). The presence of negative zonal stretching deformation areas off the EBr coast (see [Hirata and Grimm 2016](#); [Rodrigues and Woollings 2017](#)), reinforced by the stronger westerly winds during the events, results in areas with absorption of wave energy that further reduce the RW propagation. This seems in contradiction to results in [van der Wiel et al. \(2015\)](#) showing that the vorticity tendency produced by the SACZ convection is not enough to dissipate the RW and enables continued equatorward propagation beyond the convection axes. This apparent disagreement between the results is partly related to the location of convection and consequent divergence, which is due to the different EOF-based sampling approach used in [van der Wiel et al. \(2015\)](#). In their study, the core convective activity is located over southern Brazil while here the convection associated with the cloud band is located more equatorward—compare the left column of Fig. 4 herein to Fig. 5b in [van der Wiel et al. \(2015\)](#)—over the EBr coast and more directly in the main SACZ center of action. This also demonstrates the advantages of the object-based algorithm used here that directly identifies events in physical space that are free from the spatial constraints imposed by the orthogonality in traditional EOF analysis. The effects of these constraints are further exacerbated in cases with event samples based on the single principal components, especially when they are best described by mixtures of the leading EOFs.

The anticyclonic vorticity tendencies over western SATl are also a potential source for downstream RW. Its location close to the subtropical waveguide (light blue shades in Fig. 12a; see also shading in Fig. 5c) supports the eastward propagation of the disturbances across SATl and could favor the development of synoptic events over southern Africa ([Grimm and Reason 2015](#); [Rodrigues and Woollings 2017](#)). Similar RW generation is observed when the South Pacific convergence zone is active, strengthening the subtropical high over the western South Pacific

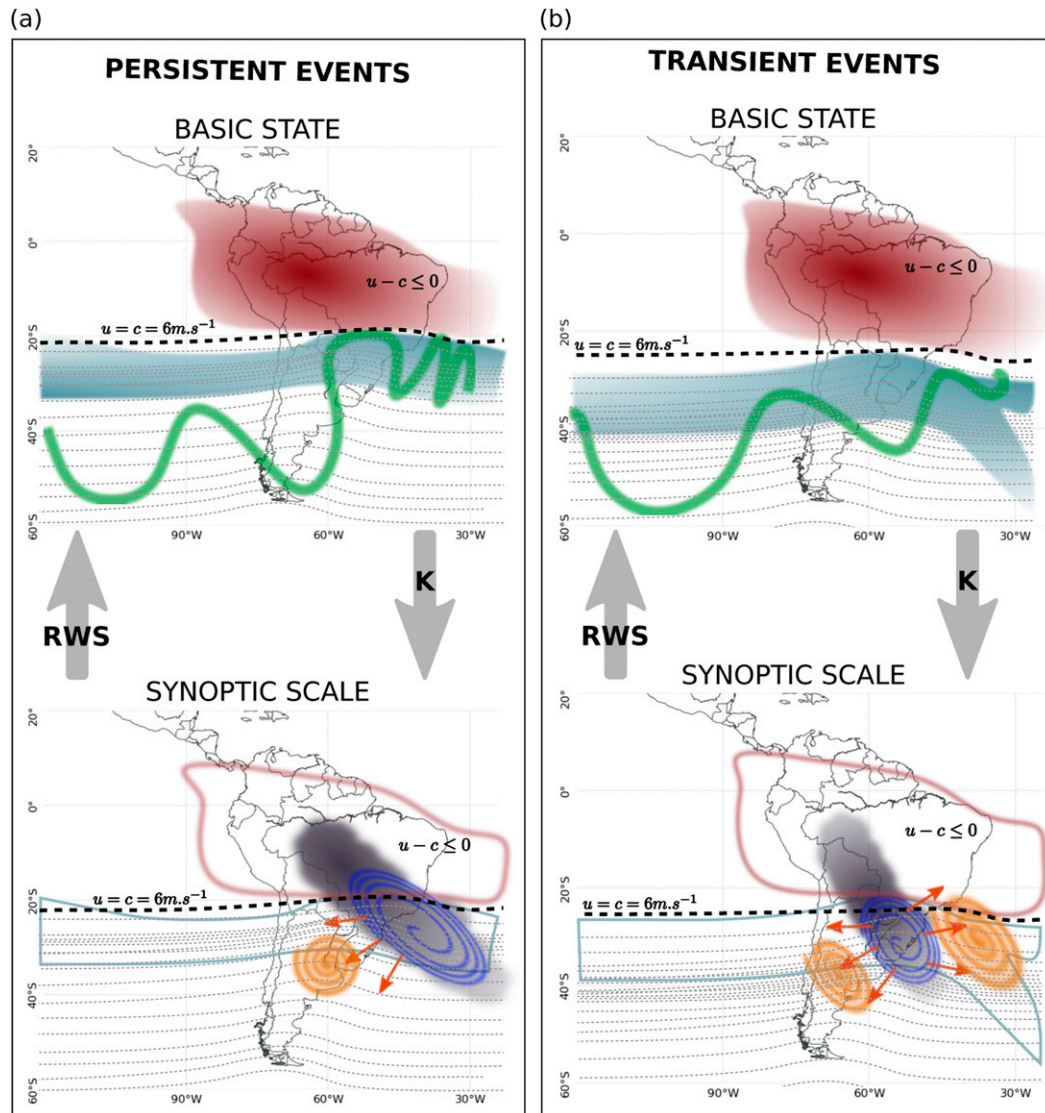


FIG. 12. Schematic with the main features associated with (a) persistent and (b) transient cloud band events, indicating the interactions between (top) the basic state and (bottom) the synoptic scale. The dotted lines indicate the areas with westerly winds at 200 hPa, with the distance between the lines representing the zonal wind speed. The black dotted line represent the location of the critical line ($u = 6 \text{ m s}^{-1}$). Equatorward of this line, the prevailing winds are easterlies ($u - c \leq 0$; red area). The light blue region indicates the average position of the subtropical waveguide and the green thick line suggest the path of the extratropical disturbances. The gray shades indicate the areas with enhanced convection, with the orange arrows representing the upper-level divergent winds and the blue (yellow) spiral representing positive (negative) RWS'.

(Fahad et al. 2021) and modulating the SACZ activity (Grimm and Silva Dias 1995).

b. Transient events

In months with enhanced transient event activity, the eastward expansion of the BH and resulting easterly wind anomalies (red shading in Fig. 12b, top) shift the critical line poleward (black dotted line in Fig. 12b, top), blocking the equatorward propagation of synoptic-scale disturbances. Additionally, the entrance of the STJ is displaced westward,

increasing the meridional anticyclonic shear south of $\sim 25^\circ$ (dotted gray lines in Fig. 12b, top), supporting anticyclonic RW breaking over SESA.

On synoptic scales, the convection associated with transient events is located farther south (gray shades in Fig. 12b, bottom). The upper-level anticyclonic anomalies resulting from this convection accelerate the STJ and increase the anticyclonic meridional shear (dotted gray lines in Fig. 12b, bottom), contributing to the dissipation of the circulation anomalies (thick green line in Fig. 12b, top). Throughout the rainy season,

the locations of the circulation anomalies are similar to subtropical South America blocking events described by [Rodrigues and Woollings \(2017\)](#), which prevent the development of the SACZ and have been related to the occurrence of droughts over SEBr.

Even though the anticyclonic vorticity tendencies resulting from the subtropical convection are stronger than during persistent events, they counteract the climatology, resulting in smaller and more confined areas of RW sources (blue spiral in [Fig. 12b](#), bottom). Furthermore, the advection across the strong vorticity gradient produces areas of cyclonic vorticity tendencies, especially over subtropical SATl (yellow spirals in [Fig. 12b](#), bottom). These areas act as RW sinks that limit downstream propagation of potential disturbances initiated by the transient events.

Thus, the location of the convection affects the local circulation and modulates whether the RW propagating over SAM will cross the SATl or will dissipate along the coast. The mechanisms explored here build upon previous studies focusing on the interaction of extratropical disturbances and convection over SAM ([Liebmann et al. 1999](#); [Nieto-Ferreira et al. 2011](#); [van der Wiel et al. 2015](#); [Rodrigues and Woollings 2017](#)). During persistent events, the extratropical disturbances reach tropical latitudes where they stall. The location of the convection also favors vorticity tendencies that act as a source of RW. During transient events, a more subtropical location of the convection, and consequent advection of vorticity, result in a dampening effect of the RW.

These results demonstrate the importance of the extratropical circulation interacting with subtropical forcing in the development and persistence of the cloud band events. The role of the tropical and local forcings can also be addressed through the sample-based approach. For example, what are the drivers behind the zonal wind anomalies over subtropical SAM? Previous studies indicate that the presence of easterly winds over the region determines the intensity of the LLJ and the active and break phases of the South American monsoon system ([Jones and Carvalho 2002](#)). The results presented here suggest an influence of the BH and LLJ, which could be further explored through an in-depth analysis of thermodynamic mechanisms and land surface processes associated with the tropical and subtropical convection.

The framework adopted is a powerful tool in evaluating cloud band variability and current and future changes in their location and persistence. Previous studies demonstrated that both SACZ activity ([Carvalho et al. 2004](#); [Cunningham and Cavalcanti 2006](#); [Hirata and Grimm 2016](#); [Vera et al. 2018](#); [Grimm 2019](#)) and blocking events leading to its absence ([Rodrigues and Woollings 2017](#)) are modulated by intraseasonal and interannual variability. Large-scale climatic modes that modify the tropical convection over the Eastern Hemisphere have well-documented influence on the basic state over South America through the sustained generation of longwave RW ([Liebmann et al. 1999](#)) and changes in convection over the Amazon and the BH ([Carvalho et al. 2004](#); [Grimm and Saboia 2015](#); [Grimm 2019](#)). Results in this study demonstrate how these monthly to interdecadal modes would influence synoptic-scale wave

propagation and the resultant tropical–extratropical cloud bands. Furthermore, previous studies have suggested a poleward migration of the SACZ in recent years ([Zilli et al. 2019](#)), resulting in an increase in the intensity of summer precipitation but a reduction in the number of rainy days over SEBr ([Zilli et al. 2017](#)). The cloud band event set developed in this study and the illustration of the impact of subtle changes in subtropical upper-level winds in favoring persistent or transient cloud bands together offer new approaches to understand the mechanisms of these changes.

8. Conclusions

In the present research, we propose a novel methodology to identify tropical–extratropical cloud band events occurring over SAM, responsible for more than 60% of the rainy season precipitation, and understand their interactions with the regional circulation. In addition to being a straightforward framework to identify SACZ events—which are essentially persistent cloud bands—it also highlighted the importance of transient events to the rainfall climatology, especially over SESA where they represent up to 30% of the total precipitation during summer.

The location, duration, and persistence of the cloud band events are controlled by the interplay of tropical convection, extratropical transients, and local surface processes across different temporal scales. The framework adopted revealed valuable information about the role of extratropical disturbances on the development and persistence of cloud bands. Anomalies in the basic-state circulation modulate the equatorward propagation of the synoptic-scale extratropical disturbances, which modifies the location and persistence of the cloud bands over SAM. The results indicate that the upper-level zonal winds are partially modulated by the BH expansion, indicating the importance of the tropical convection in setting the climatology of cloud bands.

Results here have also diagnosed, at the event scale, that the anomalous subtropical convection from the cloud bands interacts strongly with the basic flow, resulting in downwind enhancement or damping of the extratropical disturbances. During persistent events, the subtropical convection is located closer to the tropics with intense deep convection resulting in anticyclonic vorticity tendencies that slow down the approaching RW, increasing its persistence over the region. Additionally, the subtropical convection is a potential RW source for downstream wave propagation. The small magnitude of the anomalies during these events, especially in December and January, highlights their importance in maintaining the climatology since the composites are not substantially different from the monthly mean state. Conversely, during transient events, the convection is located over subtropical latitudes, with the compensatory subsidence curbing the RW propagation and resulting in short-lived events. Such interaction between scales (i.e., basic state influencing and being modified by the synoptic disturbances) is consistent with the conceptual framework proposed by [Meehl et al. \(2001\)](#) and has been demonstrated for the SACZ region using the event sample-based methodology adopted here.

In conclusion, the use of the objective-based methodology provided novel insights on the role of the basic state and synoptic-scale disturbances in determining the location of tropical–extratropical cloud-band events over SAm. This analysis framework and accompanying cloud band event set opens up new avenues for research on variability and change in the South American hydroclimate.

Acknowledgments. This research was supported by the Climate Science for Services Partnership Brazil project (CSSP-Brazil) funded by the Newton Fund. NCGH also acknowledges support from the NERC/DFID-funded UMFULA project (NE/M020207/1). Results were generated using Copernicus Climate Change Service Information 2020 ECMWF Reanalysis 5 (ERA5), available at <https://www.ecmwf.int/en/forecasts/datasets/reanalysis-datasets/era5>. The Outgoing Longwave Radiation–Daily CDR used in this study can be acquired from NOAA’s National Centers for Environmental Information (<http://www.ncei.noaa.gov>) and was originally developed by Hai-Tien Lee and colleagues for NOAA’s CDR Program. Satellite-based precipitation data from TRMM version 3B42 V7 is developed and disseminated by the National Aeronautics and Space Administration (NASA) Goddard Earth Sciences Data and Information Services Center (GES DISC) and is available at https://disc.gsfc.nasa.gov/datasets/TRMM_3B42_7/summary. The observational precipitation dataset is compiled by Xavier et al. (2016) and can be accessed at <https://utexas.app.box.com/v/xavier-et-al-ijoc-data>. The observed SACZ dates are obtained from Rosso et al. (2018). The authors would also like to acknowledge the three anonymous for their valuable comments.

Data availability statement. Data used in this study are available publicly from repositories noted in the acknowledgments. The algorithm for obtaining the tropical–extratropical cloud band event set is available open-source at <https://github.com/hart-ncg/MetBot>.

REFERENCES

- Ambrizzi, T., and S. E. Ferraz, 2015: An objective criterion for determining the South Atlantic convergence zone. *Front. Environ. Sci.*, **3** (23), <https://doi.org/10.3389/fenvs.2015.00023>.
- Carvalho, L. M., and C. Jones, 2001: A satellite method to identify structural properties of mesoscale convective systems based on the maximum spatial correlation tracking technique (MASCOTTE). *J. Appl. Meteor.*, **40**, 1683–1701, [https://doi.org/10.1175/1520-0450\(2001\)040<1683:ASMTIS>2.0.CO;2](https://doi.org/10.1175/1520-0450(2001)040<1683:ASMTIS>2.0.CO;2).
- , —, and B. Liebmann, 2002: Extreme precipitation events in southeastern South America and large-scale convective patterns in the South Atlantic convergence zone. *J. Climate*, **15**, 2377–2394, [https://doi.org/10.1175/1520-0442\(2002\)015<2377:EPEISS>2.0.CO;2](https://doi.org/10.1175/1520-0442(2002)015<2377:EPEISS>2.0.CO;2).
- , —, and —, 2004: The South Atlantic convergence zone: Intensity, form, persistence, and relationships with intraseasonal to interannual activity and extreme rainfall. *J. Climate*, **17**, 88–108, [https://doi.org/10.1175/1520-0442\(2004\)017<0088:TSACZI>2.0.CO;2](https://doi.org/10.1175/1520-0442(2004)017<0088:TSACZI>2.0.CO;2).
- , A. E. Silva, C. Jones, B. Liebmann, P. L. Dias, and H. R. Rocha, 2011: Moisture transport and intraseasonal variability in the South America monsoon system. *Climate Dyn.*, **36**, 1865–1880, <https://doi.org/10.1007/s00382-010-0806-2>.
- Cavalcanti, I. F. A., 2012: Large scale and synoptic features associated with extreme precipitation over South America: A review and case studies for the first decade of the 21st century. *Atmos. Res.*, **118**, 27–40, <https://doi.org/10.1016/j.atmosres.2012.06.012>.
- Coelho, C. A. S., D. H. Cardoso, and M. A. Firpo, 2016a: Precipitation diagnostics of an exceptionally dry event in São Paulo, Brazil. *Theor. Appl. Climatol.*, **125**, 769–784, <https://doi.org/10.1007/s00704-015-1540-9>.
- , and Coauthors, 2016b: The 2014 southeast Brazil austral summer drought: Regional scale mechanisms and teleconnections. *Climate Dyn.*, **46**, 3737–3752, <https://doi.org/10.1007/s00382-015-2800-1>.
- Cunningham, C. A. C., and I. F. A. Cavalcanti, 2006: Intraseasonal modes of variability affecting the South Atlantic convergence zone. *Int. J. Climatol.*, **26**, 1165–1180, <https://doi.org/10.1002/joc.1309>.
- Dawson, A., 2016: Windspharm: A high-level library for global wind field computations using spherical harmonics. *J. Open Res. Software*, **4**, e31, <https://doi.org/10.5334/jors.129>.
- de Quadro, M. F. L., 1994: Case study of the South Atlantic convergence zone (SACZ) over South America (in Portuguese). M.S. thesis, Dept. of Meteorology, National Institute of Space Research, 124 pp.
- Escobar, G. C. J., 2019: South Atlantic convergence zone (SACZ): Detection criteria for Weather Forecast Operational Centres (in Portuguese). INPE Tech. Rep., Instituto Nacional de Pesquisas Espaciais, 19 pp., accessed 23 September 2020, <http://urlib.net/8JMKD3MGP3W34R/3SGMUDP>.
- Fahad, A. A., N. J. Burls, E. T. Swenson, and D. M. Straus, 2021: The influence of South Pacific convergence zone heating on the South Pacific subtropical anticyclone. *J. Climate*, **34**, 3787–3798, <https://doi.org/10.1175/JCLI-D-20-0509.1>.
- Figueroa, S. N., P. Satyamurty, and P. L. Da Silva Dias, 1995: Simulations of the summer circulation over the South American region with an eta coordinate model. *J. Atmos. Sci.*, **52**, 1573–1584, [https://doi.org/10.1175/1520-0469\(1995\)052<1573:SOTSCO>2.0.CO;2](https://doi.org/10.1175/1520-0469(1995)052<1573:SOTSCO>2.0.CO;2).
- Gandu, A. W., and P. L. Silva Dias, 1998: Impact of tropical heat sources on the South American tropospheric upper circulation and subsidence. *J. Geophys. Res.*, **103**, 6001–6015, <https://doi.org/10.1029/97JD03114>.
- Gonzalez, P. L. M., and C. Vera, 2014: Summer precipitation variability over South America on long and short intraseasonal timescales. *Climate Dyn.*, **43**, 1993–2007, <https://doi.org/10.1007/s00382-013-2023-2>.
- Grimm, A. M., 2019: Madden–Julian oscillation impacts on South American summer monsoon season: Precipitation anomalies, extreme events, teleconnections, and role in the MJO cycle. *Climate Dyn.*, **53**, 907–932, <https://doi.org/10.1007/s00382-019-04622-6>.
- , and P. L. Silva Dias, 1995: Analysis of tropical–extratropical interactions with influence functions of a barotropic model. *J. Atmos. Sci.*, **52**, 3538–3555, [https://doi.org/10.1175/1520-0469\(1995\)052<3538:AOTIW1>2.0.CO;2](https://doi.org/10.1175/1520-0469(1995)052<3538:AOTIW1>2.0.CO;2).
- , and M. T. Zilli, 2009: Interannual variability and seasonal evolution of summer monsoon rainfall in South America. *J. Climate*, **22**, 2257–2275, <https://doi.org/10.1175/2008JCLI2345.1>.
- , and C. J. C. Reason, 2015: Intraseasonal teleconnections between South America and South Africa. *J. Climate*, **28**, 9489–9497, <https://doi.org/10.1175/JCLI-D-15-0116.1>.
- , and J. P. Saboia, 2015: Interdecadal variability of the South American precipitation in the monsoon season. *J. Climate*, **28**, 755–775, <https://doi.org/10.1175/JCLI-D-14-00046.1>.

- Harrison, M. S. J., 1984: A generalized classification of South African summer rain-bearing synoptic systems. *J. Climatol.*, **4**, 547–560, <https://doi.org/10.1002/joc.3370040510>.
- Hart, N. C. G., C. J. C. Reason, and N. Fauchereau, 2010: Tropical–extratropical interactions over southern Africa: Three cases of heavy summer season rainfall. *Mon. Wea. Rev.*, **138**, 2608–2623, <https://doi.org/10.1175/2010MWR3070.1>.
- , —, and —, 2012: Building a tropical–extratropical cloud band metbot. *Mon. Wea. Rev.*, **140**, 4005–4016, <https://doi.org/10.1175/MWR-D-12-00127.1>.
- , R. Washington, and C. J. C. Reason, 2018: On the likelihood of tropical–extratropical cloud bands in the south Indian convergence zone during ENSO events. *J. Climate*, **31**, 2797–2817, <https://doi.org/10.1175/JCLI-D-17-0221.1>.
- Hersbach, H., and Coauthors, 2020: The ERA5 global reanalysis. *Quart. J. Roy. Meteor. Soc.*, **146**, 1999–2049, <https://doi.org/10.1002/qj.3803>.
- Hirata, F. E., and A. M. Grimm, 2016: The role of synoptic and intraseasonal anomalies in the life cycle of summer rainfall extremes over South America. *Climate Dyn.*, **46**, 3041–3055, <https://doi.org/10.1007/s00382-015-2751-6>.
- Hoskins, B. J., and D. J. Karoly, 1981: The steady linear response of a spherical atmosphere to thermal and orographic forcing. *J. Atmos. Sci.*, **38**, 1179–1196, [https://doi.org/10.1175/1520-0469\(1981\)038<1179:TSLROA>2.0.CO;2](https://doi.org/10.1175/1520-0469(1981)038<1179:TSLROA>2.0.CO;2).
- , and T. Ambrizzi, 1993: Rossby wave propagation on a realistic longitudinally varying flow. *J. Atmos. Sci.*, **50**, 1661–1671, [https://doi.org/10.1175/1520-0469\(1993\)050<1661:RWPOAR>2.0.CO;2](https://doi.org/10.1175/1520-0469(1993)050<1661:RWPOAR>2.0.CO;2).
- Huffman, G. J., E. F. Stocker, D. T. Bolvin, E. J. Nelkin, and R. F. Adler, 2014: TRMM (TMPA) Rainfall Estimate L3 3 hour 0.25 degree \times 0.25 degree V7. Goddard Earth Sciences Data and Information Services Center (GES DISC), Greenbelt, MD, accessed 26 September 2016, <https://doi.org/10.5067/TRMM/TMPA/3H/7>.
- Jones, C., and L. M. Carvalho, 2002: Active and break phases in the South American monsoon system. *J. Climate*, **15**, 905–914, [https://doi.org/10.1175/1520-0442\(2002\)015<0905:AABPIT>2.0.CO;2](https://doi.org/10.1175/1520-0442(2002)015<0905:AABPIT>2.0.CO;2).
- Karoly, D. J., 1983: Rossby wave propagation in a barotropic atmosphere. *Dyn. Atmos. Oceans*, **7**, 111–125, [https://doi.org/10.1016/0377-0265\(83\)90013-1](https://doi.org/10.1016/0377-0265(83)90013-1).
- Kiladis, G. N., H. von Storch, and H. Loon, 1989: Origin of the South Pacific convergence zone. *J. Climate*, **2**, 1185–1195, [https://doi.org/10.1175/1520-0442\(1989\)002<1185:OOTSPC>2.0.CO;2](https://doi.org/10.1175/1520-0442(1989)002<1185:OOTSPC>2.0.CO;2).
- Kodama, Y., 1992: Large-scale common features of subtropical precipitation zones (the baiu frontal zone, the SPCZ, and the SACZ) Part I: Characteristics of subtropical frontal zones. *J. Meteor. Soc. Japan*, **70**, 813–836, https://doi.org/10.2151/jmsj1965.70.4_813.
- , 1993: Large-scale common features of sub-tropical convergence zones (the baiu frontal zone, the SPCZ, and the SACZ) Part II: Conditions of the circulations for generating the STCZs. *J. Meteor. Soc. Japan*, **71**, 581–610, https://doi.org/10.2151/jmsj1965.71.5_581.
- Lee, H.-T., 2014: Climate algorithm theoretical basis document (C-ATBD): Outgoing longwave radiation (OLR)—daily. NOAA’s Climate Data Record (CDR) Program Tech. Rep. CDRP-ATBD-0526, NOAA, accessed 6 November 2019, https://www1.ncdc.noaa.gov/pub/data/sds/cdr/CDRs/Outgoing%20Longwave%20Radiation%20-%20Daily/AlgorithmDescription_01B-21.pdf.
- , and NOAA-CDR Program, 2011: NOAA Climate Data Record (CDR) of daily outgoing longwave radiation (OLR), version 1.2. NOAA National Climatic Data Center, accessed 6 November 2019, <https://doi.org/10.7289/V5SJ1HH2>.
- Lenters, J. D., and K. H. Cook, 1997: On the origin of the Bolivian high and related circulation features of the South American climate. *J. Atmos. Sci.*, **54**, 656–678, [https://doi.org/10.1175/1520-0469\(1997\)054<0656:OTOOTB>2.0.CO;2](https://doi.org/10.1175/1520-0469(1997)054<0656:OTOOTB>2.0.CO;2).
- Liebmann, B., G. N. Kiladis, J. A. Marengo, T. Ambrizzi, and J. D. Glick, 1999: Submonthly convective variability over South America and the South Atlantic convergence zone. *J. Climate*, **12**, 1877–1891, [https://doi.org/10.1175/1520-0442\(1999\)012<1877:SCVOSA>2.0.CO;2](https://doi.org/10.1175/1520-0442(1999)012<1877:SCVOSA>2.0.CO;2).
- Lintner, B. R., and J. D. Neelin, 2010: Tropical South America–Atlantic sector convective margins and their relationship to low-level inflow. *J. Climate*, **23**, 2671–2685, <https://doi.org/10.1175/2009JCLI3301.1>.
- Mattingly, K. S., and T. L. Mote, 2017: Variability in warm-season atmospheric circulation and precipitation patterns over subtropical South America: Relationships between the South Atlantic convergence zone and large-scale organized convection over the La Plata basin. *Climate Dyn.*, **48**, 241–263, <https://doi.org/10.1007/s00382-016-3072-0>.
- Meehl, M., R. Lukas, G. N. Kiladis, K. M. Weickmann, A. J. Matthews, and M. Wheeler, 2001: A conceptual framework for time and space scale interactions in the climate system. *Climate Dyn.*, **17**, 753–775, <https://doi.org/10.1007/s003820000143>.
- Monahan, A. H., J. C. Fyfe, M. H. Ambaum, D. B. Stephenson, and G. R. North, 2009: Empirical orthogonal functions: The medium is the message. *J. Climate*, **22**, 6501–6514, <https://doi.org/10.1175/2009JCLI3062.1>.
- Nielsen, D. M., A. L. Belém, E. Marton, and M. Cataldi, 2019: Dynamics-based regression models for the South Atlantic convergence zone. *Climate Dyn.*, **52**, 5527–5553, <https://doi.org/10.1007/s00382-018-4460-4>.
- Nieto-Ferreira, R., T. M. Rickenbach, and E. A. Wright, 2011: The role of cold fronts in the onset of the monsoon season in the South Atlantic convergence zone. *Quart. J. Roy. Meteor. Soc.*, **137**, 908–922, <https://doi.org/10.1002/qj.810>.
- Nogués-Paegle, J., and K. C. Mo, 1997: Alternating wet and dry conditions over South America during summer. *Mon. Wea. Rev.*, **125**, 279–291, [https://doi.org/10.1175/1520-0493\(1997\)125<0279:AWADCO>2.0.CO;2](https://doi.org/10.1175/1520-0493(1997)125<0279:AWADCO>2.0.CO;2).
- Qin, J., and W. A. Robinson, 1993: On the Rossby wave source and the steady linear response to tropical forcing. *J. Atmos. Sci.*, **50**, 1819–1823, [https://doi.org/10.1175/1520-0469\(1993\)050<1819:OTRWSA>2.0.CO;2](https://doi.org/10.1175/1520-0469(1993)050<1819:OTRWSA>2.0.CO;2).
- Robertson, A. W., and C. R. Mechoso, 2000: Interannual and interdecadal variability of the South Atlantic convergence zone. *Mon. Wea. Rev.*, **128**, 2947–2957, [https://doi.org/10.1175/1520-0493\(2000\)128<2947:IAIVOT>2.0.CO;2](https://doi.org/10.1175/1520-0493(2000)128<2947:IAIVOT>2.0.CO;2).
- Rodrigues, R. R., and T. Woollings, 2017: Impact of atmospheric blocking on South America in austral summer. *J. Climate*, **30**, 1821–1837, <https://doi.org/10.1175/JCLI-D-16-0493.1>.
- , A. S. Taschetto, A. Sen Gupta, and G. R. Foltz, 2019: Common cause for severe droughts in South America and marine heatwaves in the South Atlantic. *Nat. Geosci.*, **12**, 620–626, <https://doi.org/10.1038/s41561-019-0393-8>.
- Rosa, E. B., L. P. Pezzi, M. F. L. de Quadros, and N. Brunsell, 2020: Automated detection algorithm for SACZ, oceanic SACZ, and their climatological features. *Front. Environ. Sci.*, **8**, 18, <https://doi.org/10.3389/fenvs.2020.00018>.
- Rosso, F., N. Boiaski, S. Ferraz, and T. Robles, 2018: Influence of the Antarctic Oscillation on the South Atlantic convergence zone. *Atmosphere*, **9**, 431, <https://doi.org/10.3390/atmos9110431>.

- Sardeshmukh, P. D., and B. J. Hoskins, 1988: The generation of global rotational flow by steady idealized tropical divergence. *J. Atmos. Sci.*, **45**, 1228–1251, [https://doi.org/10.1175/1520-0469\(1988\)045<1228:TGOGRF>2.0.CO;2](https://doi.org/10.1175/1520-0469(1988)045<1228:TGOGRF>2.0.CO;2).
- Shimizu, M. H., and I. F. A. de Cavalcanti, 2011: Variability patterns of Rossby wave source. *Climate Dyn.*, **37**, 441–454, <https://doi.org/10.1007/s00382-010-0841-z>.
- Thorncroft, C. D., B. J. Hoskins, and M. E. McIntyre, 1993: Two paradigms of baroclinic-wave life-cycle behaviour. *Quart. J. Roy. Meteor. Soc.*, **119**, 17–55, <https://doi.org/10.1002/qj.49711950903>.
- Todd, M., R. Washington, and T. James, 2003: Characteristics of summertime daily rainfall variability over South America and the South Atlantic convergence zone. *Meteor. Atmos. Phys.*, **83**, 89–108, <https://doi.org/10.1007/s00703-002-0563-9>.
- van der Wiel, K., A. J. Matthews, D. P. Stevens, and M. M. Joshi, 2015: A dynamical framework for the origin of the diagonal South Pacific and South Atlantic convergence zones. *Quart. J. Roy. Meteor. Soc.*, **141**, 1997–2010, <https://doi.org/10.1002/qj.2508>.
- Vera, C., and Coauthors, 2006: Toward a unified view of the American monsoon systems. *J. Climate*, **19**, 4977–5000, <https://doi.org/10.1175/JCLI3896.1>.
- , M. S. Alvarez, P. L. Gonzalez, B. Liebmann, and G. N. Kiladis, 2018: Seasonal cycle of precipitation variability in South America on intraseasonal timescales. *Climate Dyn.*, **51**, 1991–2001, <https://doi.org/10.1007/s00382-017-3994-1>.
- Vincent, D. G., 1994: The South Pacific convergence zone (SPCZ): A review. *Mon. Wea. Rev.*, **122**, 1949–1970, [https://doi.org/10.1175/1520-0493\(1994\)122<1949:TSPCZA>2.0.CO;2](https://doi.org/10.1175/1520-0493(1994)122<1949:TSPCZA>2.0.CO;2).
- Washington, R., and M. Todd, 1999: Tropical–temperate links in southern Africa and southwest Indian Ocean satellite-derived daily rainfall. *Int. J. Climatol.*, **19**, 1601–1616, [https://doi.org/10.1002/\(SICI\)1097-0088\(19991130\)19:14<1601::AID-JOC407>3.0.CO;2-0](https://doi.org/10.1002/(SICI)1097-0088(19991130)19:14<1601::AID-JOC407>3.0.CO;2-0).
- Wilks, D., 2011a: Frequentist statistical inference. *Statistical Methods in the Atmospheric Sciences*, 3rd ed., Academic Press, 133–186, <https://doi.org/10.1016/B978-0-12-385022-5.00005-1>.
- , 2011b: The multivariate normal (MVN) distribution. *Statistical Methods in the Atmospheric Sciences*, 3rd ed., Academic Press, 491–518, <https://doi.org/10.1016/B978-0-12-385022-5.00011-7>.
- Wirth, V., M. Riemer, E. K. M. Chang, and O. Martius, 2018: Rossby wave packets on the midlatitude waveguide—A review. *Mon. Wea. Rev.*, **146**, 1965–2001, <https://doi.org/10.1175/MWR-D-16-0483.1>.
- Woollings, T., and Coauthors, 2018: Daily to decadal modulation of jet variability. *J. Climate*, **31**, 1297–1314, <https://doi.org/10.1175/JCLI-D-17-0286.1>.
- Xavier, A. C., C. W. King, and B. R. Scanlon, 2016: Daily gridded meteorological variables in Brazil (1980–2013). *Int. J. Climatol.*, **36**, 2644–2659, <https://doi.org/10.1002/joc.4518>.
- Zanin, P. R., and P. Satyamurty, 2020: Hydrological processes interconnecting the two largest watersheds of South America from seasonal to intra-monthly time scales: A critical review. *Int. J. Climatol.*, **40**, 3971–4005, <https://doi.org/10.1002/joc.6443>.
- Zilli, M. T., L. M. Carvalho, B. Liebmann, and M. A. Silva Dias, 2017: A comprehensive analysis of trends in extreme precipitation over southeastern coast of Brazil. *Int. J. Climatol.*, **37**, 2269–2279, <https://doi.org/10.1002/joc.4840>.
- , —, and B. R. Lintner, 2019: The poleward shift of South Atlantic convergence zone in recent decades. *Climate Dyn.*, **52**, 2545–2563, <https://doi.org/10.1007/s00382-018-4277-1>.